CSF-contacting neurons respond to Streptococcus pneumoniae and promote host survival during central nervous system infection

Andrew Prendergast, Kin Ki Jim, Hugo Marnas, Laura Desban, Feng Quan, Lydia Djenoune, Valerio Laghi, Agnès Hocquemiller, Elias Lunsford, Julian Roussel, et al.

Article

Current Biology

CSF-contacting neurons respond to *Streptococcus pneumoniae* and promote host survival during central nervous system infection

Graphical abstract

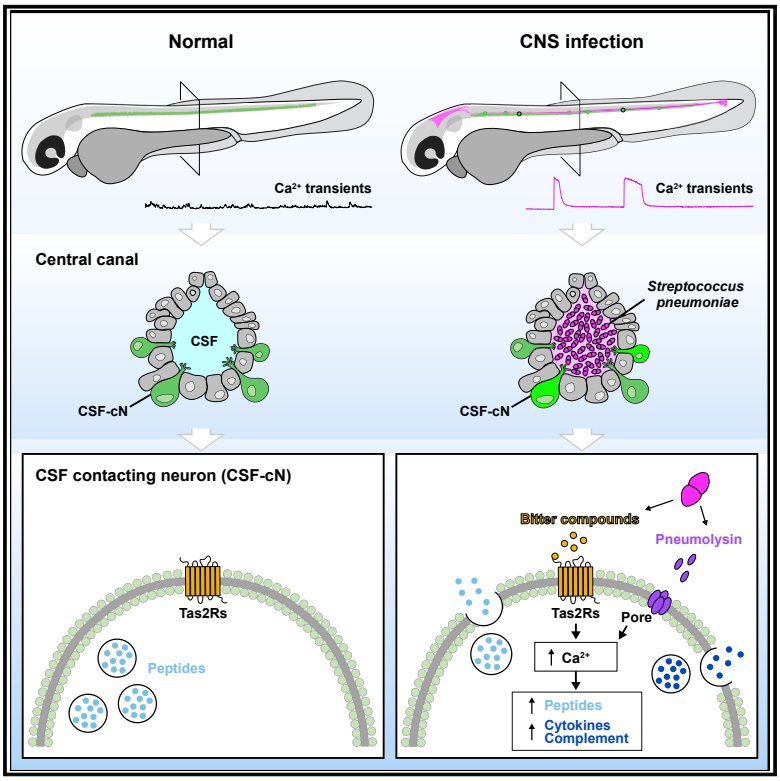

Highlights

- Infection of zebrafish with *S. pneumoniae* elicits pathognomonic signs of meningitis
- CSF-cNs show massive activation when *S. pneumoniae* invade the CSF
- Metabolites secreted by *S. pneumoniae* induce similar activation of CSF-cNs
- CSF-cN secretion increases host survival upon *S. pneumoniae* infection

Authors

Andrew E. Prendergast, Kin Ki Jim, Hugo Marnas, ..., Diederik van de Beek, Christina M.J.E. Vandenbroucke-Grauls, Claire Wyart

Correspondence

vandenbrouckegrauls@amsterdamumc.nl (C.M.J.E.V.-G.), claire.wyart@icm-institute.org (C.W.)

In brief

Prendergast et al. discover that cerebrospinal fluid-contacting neurons (CSF-cNs), which are known to detect spinal curvature and control posture, also respond to bacterial metabolites, and during infections of the central nervous system, they secrete compounds that promote host survival.

Prendergast et al., 2023, Current Biology *33*, 940–956
March 13, 2023
https://doi.org/10.1016/j.cub.2023.01.039

CellPress

CellPress
OPEN ACCESS

Current Biology

Article

CSF-contacting neurons respond to *Streptococcus pneumoniae* and promote host survival during central nervous system infection

Andrew E. Prendergast,[1,9,10] Kin Ki Jim,[2,3,4,5,10] Hugo Marnas,[1,10] Laura Desban,[1] Feng B. Quan,[1] Lydia Djenoune,[1] Valerio Laghi,[6] Agnès Hocquemiller,[1] Elias T. Lunsford,[1] Julian Roussel,[1] Ludovic Keiser,[7] Francois-Xavier Lejeune,[1] Mahalakshmi Dhanasekar,[1] Pierre-Luc Bardet,[1] Jean-Pierre Levraud,[6,8] Diederik van de Beek,[2,3] Christina M.J.E. Vandenbroucke-Grauls,[4,5,*] and Claire Wyart[1,11,*]

[1]Institut du Cerveau (ICM), Sorbonne Université, UPMC Univ Paris 06, Inserm, CNRS, AP-HP, Hôpital Pitié-Salpêtrière, 47 Boulevard de l'Hôpital, 75013 Paris, France
[2]Amsterdam UMC location University of Amsterdam, Department of Neurology, Meibergdreef 9, 1105 AZ Amsterdam, the Netherlands
[3]Amsterdam Neuroscience, 1081 HV Amsterdam, the Netherlands
[4]Amsterdam UMC location Vrije Universiteit Amsterdam, Department of Medical Microbiology and Infection Prevention, De Boelelaan 1117, 1081 HV Amsterdam, the Netherlands
[5]Amsterdam Institute for Infection and Immunity, 1081 HV Amsterdam, the Netherlands
[6]Institut Pasteur, Unité Macrophages et Développement, Centre National de la Recherche Scientifique (CNRS), Université Paris-Cité, 75015 Paris, France
[7]Ecole Polytechnique Fédérale de Lausanne (EPFL), Station 18, 1015 Lausanne, Switzerland
[8]Université Paris-Saclay, CNRS, Institut Pasteur, Université Paris-Cité, Institut des Neurosciences Paris-Saclay, 91400 Saclay, France
[9]Present address: Yale Zebrafish Research Core, Yale University, New Haven, CT 06511, USA
[10]These authors contributed equally
[11]Lead contact
*Correspondence: vandenbrouckegrauls@amsterdamumc.nl (C.M.J.E.V.-G.), claire.wyart@icm-institute.org (C.W.)
https://doi.org/10.1016/j.cub.2023.01.039

SUMMARY

The pathogenic bacterium *Streptococcus pneumoniae* (*S. pneumoniae*) can invade the cerebrospinal fluid (CSF) and cause meningitis with devastating consequences. Whether and how sensory cells in the central nervous system (CNS) become activated during bacterial infection, as recently reported for the peripheral nervous system, is not known. We find that CSF infection by *S. pneumoniae* in larval zebrafish leads to changes in posture and behavior that are reminiscent of pneumococcal meningitis, including dorsal arching and epileptic-like seizures. We show that during infection, invasion of the CSF by *S. pneumoniae* massively activates *in vivo* sensory neurons contacting the CSF, referred to as "CSF-cNs" and previously shown to detect spinal curvature and to control posture, locomotion, and spine morphogenesis. We find that CSF-cNs express orphan bitter taste receptors and respond *in vitro* to bacterial supernatant and metabolites via massive calcium transients, similar to the ones observed *in vivo* during infection. Upon infection, CSF-cNs also upregulate the expression of numerous cytokines and complement components involved in innate immunity. Accordingly, we demonstrate, using cell-specific ablation and blockade of neurotransmission, that CSF-cN neurosecretion enhances survival of the host during *S. pneumoniae* infection. Finally, we show that CSF-cNs respond to various pathogenic bacteria causing meningitis in humans, as well as to the supernatant of cells infected by a neurotropic virus. Altogether, our work uncovers that central sensory neurons in the spinal cord, previously involved in postural control and morphogenesis, contribute as well to host survival by responding to the invasion of the CSF by pathogenic bacteria during meningitis.

INTRODUCTION

During a bacterial infection of the skin, bacteria invading the subcutaneous tissues can directly activate nociceptor sensory neurons through N-formyl peptides and pore-forming toxins, contributing to inflammation and innate immunity by releasing regulatory neuropeptides.[1] A similar phenomenon occurs in the respiratory epithelium where ciliated epithelial cells detect bacterial metabolites and induce an inflammatory response.[2] During bacterial infection of the central nervous system (CNS), bacteria invade the cerebrospinal fluid (CSF) that circulates from the brain ventricles down to the central canal of the spinal cord. We hypothesized that bacteria in the CNS could similarly induce activation of sensory neurons in contact with the CSF.

Along the walls of the central canal in the spinal cord, sensory cells—referred to as CSF-contacting neurons (CSF-cNs)—are numerous across vertebrate species.[3,4] Our group and others have shown over the last decade that these cells are

CellPress
OPEN ACCESS

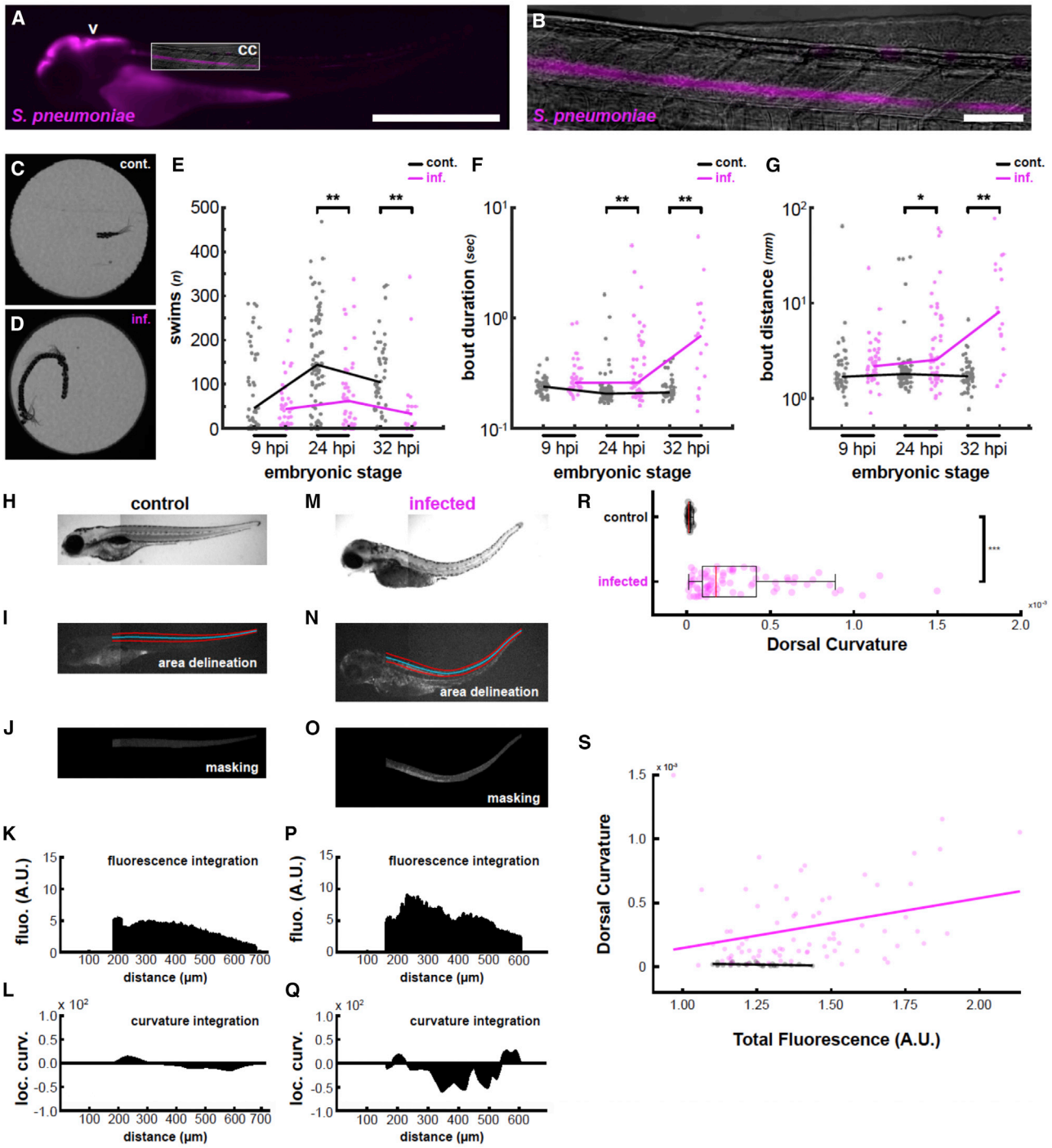

Figure 1. Infection induces behavioral changes and spinal curvature reminiscent of clinical symptoms of pneumococcal meningitis

(A) Fluorescence image of a larva infected with mCherry-labeled *S. pneumoniae* at 2 dpf and imaged at 24 hpi showing colonization of the brain ventricle (v) and central canal (cc). Box indicates field of view for (B). Scale bars, 500 μm.

(B) Higher magnification image of the central canal colonized with mCherry-labeled *S. pneumoniae*. Scale bars, 50 μm.

(C) Representative motion overlay of a detected swim bout from a larva injected with vehicle. Most bouts are short forward swims.

(D) Representative motion overlay of a detected swim bout from a larva infected with *S. pneumoniae*. These swim bouts tend to be much longer in duration and distance.

(E) Quantification of the overall number of bouts in PBS-injected (gray) and *S. pneumoniae*-infected (magenta) fish at three different time points post infection. At later infection time points, infected fish swim substantially less often (**$p < 0.01$).

(legend continued on next page)

interoceptive ciliated mechanosensory neurons that detect spinal curvature[5–8] and in turn release GABA to optimize the kinematics of locomotion[9] and active posture[10,11] in the short timescale as well as morphogenesis throughout life.[12,13] In particular, the release of peptides from the urotensin family by ventral CSF-cNs elicits dorsalward arching via contraction of the dorsal musculature.[12,14–19] CSF-cNs express the transient receptor channel PKD2L1[20,21] that enables them to detect changes in pH and osmolarity.[20–22] We hypothesize that these CSF-cNs could be recruited due to changes in CSF content during CNS infection, in order to modulate the inflammatory and immune response, and possibly contribute to changes in neck stiffness and posture seen in meningitis patients.[23] To investigate this hypothesis, we took advantage of a model of pneumococcal meningitis developed in larval zebrafish.[24] We used *Streptococcus pneumoniae* (*S. pneumoniae*) as it is the most common cause of community-acquired bacterial meningitis worldwide[25–28] and is associated with high mortality and morbidity rates despite the introduction of conjugate vaccines.[25] We therefore injected *S. pneumoniae* in the hindbrain ventricles (HBVs) of transgenic larval zebrafish expressing the fluorescent genetically encoded calcium sensor GCaMP under the *pkd2l1* promoter.

Supporting our hypothesis, we observed that CNS infection by *S. pneumoniae* in zebrafish larvae led to phenotypes reminiscent of pneumococcal meningitis in humans, including dorsal arching and epileptic-like seizures. In this model, we established a live calcium imaging approach to monitor the activation of CSF-cNs upon injection of *S. pneumoniae* in the brain ventricles. We discovered that CSF-cNs are activated when pathogenic bacteria invade the CSF, as shown by large and long-lasting calcium transients. We show that similarly large calcium transients in CSF-cNs can be elicited *in vitro* by exposure to microbial metabolites acting as bitter compounds. Accordingly, we find that CSF-cNs specifically express orphan bitter taste receptors along with neuropeptides with antimicrobial or immunomodulatory functions. Upon infection, CSF-cNs upregulate the expression of numerous cytokines and complement components. Finally, blocking the neurosecretion of CSF-cNs or ablating these cells reduces host survival upon infection. The massive activation of CSF-cNs in response to *S. pneumoniae* occurs for other bacterial and viral pathogens as well, suggesting their function as tasters of the CSF in the context of infection is widespread. Our study demonstrates that central sensory neurons respond to products of pathogenic bacteria, are recruited during pneumococcal infection of the CNS, and furthermore confer a survival benefit. We conclude that CSF-cNs are not only mechanosensory cells detecting spinal curvature to modulate locomotion, posture, and morphogenesis, but they also act akin to taste receptor cells and contribute to innate immunity during CNS infection.

RESULTS

Zebrafish larvae infected with *S. pneumoniae* exhibit phenotypes reminiscent of clinical symptoms of pneumococcal meningitis

Clinical features of pneumococcal meningitis include headache, fever, neck stiffness, and altered mental status.[29] Seizures occur in one out of five patients.[30] If left untreated by antibiotics, an extreme form of neck stiffness called opisthotonos, an abnormal posture where the back becomes extremely arched,[23] is exhibited. To validate our zebrafish model, we monitored the behavior and posture of larval zebrafish after injection of the mCherry-labeled *S. pneumoniae* D39 HlpA-mCherry strain in the HBV (Figure 1; STAR Methods). We observed that mCherry-positive pneumococci proliferate and migrate to colonize the brain ventricles and central canal over 24 h post injection (hpi) (Figures 1A and 1B). Freely swimming, vehicle-injected control larvae at 5 and 6 days post fertilization (dpf) typically explored their environment via slow locomotor bouts (Figures 1C–1G) typically occurring once a second.[31] By contrast, infected larvae swam less often (Figure 1E) as a possible reflection of sickness behavior and neuroinflammation.[32] When infected larval zebrafish swam, however, they exhibited locomotor bouts that lasted longer (Figure 1F) and covered a much larger distance traveled (Figures 1D and 1G), consistent with epileptic-like seizures occurring in ~25% of

(F) Quantification of bout duration in control versus infected fish. As infection progresses, swim bouts become substantially and progressively longer in infected fish while generally remaining stable in controls.
(G) Quantification of bout distance in control versus infected fish. Similarly to (E), infected fish swim substantially farther in a given bout than control fish (*$p < 0.05$).
(H) Bright-field image of a PBS-injected larva at 3 dpf.
(I) Spinal cord area (here in the control larva of H) was defined by manual tracing (red lines), from which a smoothing spline curve was fit (blue line).
(J) The resulting boundaries were used to isolate a masked portion of the red channel. Since this larva was not injected with fluorophores, this represents autofluorescence.
(K) The resulting image patch was summed along the x axis to derive a fluorescence plot.
(L) Curvature was locally determined along the x axis and plotted. Positive values indicate downward curvature, and negative values indicate upward curvature.
(M) Bright-field image of a larva injected with *S. pneumoniae* at 2 dpf and imaged at 32 hpi. Note the strong upward tail curvature.
(N) Similar spinal cord delineation as in (M) but applied to the larva in (K).
(O) Red channel fluorescence from the masked spinal cord of the infected larvae. Since this embryo was injected with mCherry-labeled *S. pneumoniae*, this plot provides a visual assessment of infection progression.
(P) Similar fluorescence plot as in (K). Note that fluorescence is overall higher than in (K).
(Q) Similar curvature plot as in (L). The larva's strong upward spinal curvature is reflected in the large downward deflection of the curvature plot midway along the anterior/posterior axis.
(R) Quantification of the absolute value of the curvature along the spinal cord in control (PBS) and infected fish. Infected fish exhibit significant greater spinal curvature ($p < 10^{-16}$). Red bars represent the medians. Boxplot represents IQR ± minimum/maximum sans outliers.
(S) Fluorescence was quantified along the spinal cord for all fish and plotted against overall curvature. In infected fish (in purple), there is a positive correlation between spinal fluorescence (i.e., implied infection progression) and spinal curvature ($R^2 = 0.0900$, $p = 0.0089$), while control fish (in black) do not show positive correlation ($R^2 = 0.0892$, $p = 0.1230$). n = 29 PBS-injected larvae; n = 75 *S. pneumoniae*-injected larvae.
See also Table S1.

infected fish.[33] Furthermore, the posture of infected larvae also became affected. While the body axis of vehicle-injected control larvae was reliably straight (Figures 1H–1L), infected larvae developed 24 h after the injection with *S. pneumoniae* pronounced dorsal arching (Figures 1M–1Q). The dorsal curvature remarkably scaled with the degree of bacterial invasion estimated by the fluorescence of the larvae injected with *S. pneumoniae* D39 fluorescent bacteria (observed both in red for HlpA-mCherry and green for HlpA-GFP; Figures 1R and 1S). Taken together, the reduced activity and abnormal posture in larval zebrafish whose CSF is invaded by bacteria are reminiscent of clinical features of pneumococcal meningitis.

Sensory neurons contacting the CSF respond *in vivo* to live *S. pneumoniae* invading the CSF

We know that overexpression of urotensin-related peptides (*urp1* and *urp2*) that are highly expressed by CSF-cNs[14] induces dorsal arching in zebrafish embryos and larvae.[12,14–19] We therefore hypothesize that CSF-cNs could be activated upon pneumococcal infection of the CSF. We investigated whether upon CSF pneumococcal infection, an activation of CSF-cNs could precede the occurrence of late symptom of dorsal arching (i.e., after 24 hpi). After *S. pneumoniae* injection in 2 dpf transgenic *Tg(pkd2l1:GCaMP5G)* larvae expressing GCaMP5G in CSF-cNs (STAR Methods), we monitored the activity of CSF-cNs for 24 h (Figures 2A–2D). In larvae injected with vehicle, CSF-cNs spontaneously exhibited baseline activity as small calcium transients (rarely rising above 50% ΔF/F; Figures 2C and 2E). By contrast, in infected larvae, a subset of CSF-cNs produced large and sustained calcium transients (mean maximum ΔF/F of 240%, mean duration of 13 s) (Figures 2D and 2F; Video S1). These massive calcium transients began as early as 12 hpi and continued within the same cells for several hours (Figures 2D, 2F, and 2G). Concomitant with the unusual activation of CSF-cNs in infected larvae, we observed an overall decline in baseline calcium activity relative to controls (Figure 2H). Note that under the same conditions, we did not observe recruitment of neutrophils in the CSF at the level of the central canal before 24 hpi (Figure S1), suggesting the response of CSF-cNs is due to bacteria or their products secreted in the CSF.

Determining whether active pathogenic bacteria are required to generate the observed neuronal activation during infection, we injected different bacterial preparations into the central canal. As before, the injection of vehicle did not trigger substantial CSF-cN activity and neither did the injection of non-pathogenic *E. coli* nor heat-killed *S. pneumoniae* (Figure 2I). In this series of experiments, only infection with live pathogenic pneumococci generated large CSF-cN transients ($p = 6.28E{-}16$) (Figures 2I and 2J). Taken together, these results suggest that the observed effect in CSF-cNs is specific to infection by live pneumococci.

CSF-cNs respond *in vitro* to cytolysins and microbial metabolites secreted by *S. pneumoniae*

Several meningeal pathogens produce pore-forming toxins that are major virulence factors; an example of this is the production of pneumolysin by *S. pneumoniae*.[34] Initially, we attempted to access the central canal directly via a pipette to test the response to pneumolysin *in vivo*; however, the small size of the central canal and the fact that CSF-cNs respond to mechanical stimulation[5] impeded this experiment. We therefore decided instead to test the effects of pneumolysin on a primary culture of CSF-cNs expressing the genetically encoded calcium indicator GCaMP5G together with tagRFP in the double-transgenic larvae *Tg(pkd2l1:tagRFP; pkd2l1:GCaMP5G)*.[5] By numerical simulations based on tests with pressure applications of fluorescent dyes, we estimated that during a 1-s pressure application, a CSF-cN *in vitro* is typically exposed to at most 50% of the initial concentration in the stimulation pipette, independent of the molecule's coefficient of diffusion that will only impact the decay of the chemical pulse (Figure 3A; STAR Methods). Thus, an initial concentration of 0.1 mg/mL pneumolysin diluted in artificial CSF (aCSF) leads to a transient chemical pulse of 0.05 mg/mL onto the cultured neurons (Figure 3A; rationales for doses of all applied compounds are provided in STAR Methods). In primary cultures, the focal pressure application of aCSF alone did not induce a response in CSF-cNs (Figures 3B, 3C, middle panel, and 3D; Video S2), showing that this pressure application was not sufficient to mechanically activate CSF-cNs. By contrast, exposure to 0.05 mg/mL pneumolysin led to a small and brief stimulus-locked calcium increase in CSF-cNs (median = 17.49% ± 14.51%; Figures 3B, right panel, and 3D; Video S2).

We next tested whether CSF-cNs respond to microbial metabolites secreted by *S. pneumoniae* during growth[35]—which could act as bitter compounds on taste receptor cells—similarly to what was previously shown for ciliated sensory cells in the mammalian airway epithelium.[2,36–39] Microbial metabolites secreted by *S. pneumoniae* include a number of microbial volatile organic compounds (mVOCs) that act indeed as bitter compounds, such as acetone, 2-butanone, 2-pentanone, 2-methylpropanal, dimethyl disulfide (DMDS), methylmercaptan, γ-butyrolactone, isopentanol, formaldehyde, and trimethylamine.[40,41] Exposure to a mixture of 50 mM bitter compounds, including acetone, 2-butanone, 2-pentanone, 2-methylpropanal, and DMDS, elicited large calcium transients in CSF-cNs (median ΔF/F = 101.25% ± 61%; Figures 3C and 3E–3G; Video S2; STAR Methods), an effect not observed with aCSF only (Figures 3C–3E). CSF-cN responses were larger for bitter compounds than for pneumolysin and mimicked more closely the response to live bacteria observed *in vivo*. When bitter compounds were tested individually, 2-pentanone and DMDS both induced responses (Figures 3H–3J and S2; Video S2), but only DMDS recapitulated in a dose-dependent manner the large responses observed with the mixture of compounds. This suggests that DMDS is a major bitter, metabolite-activating CSF-cN (Figure 3H). Taken together, these results show that CSF-cNs exhibited calcium responses to at least two different bacterial products: pneumolysin, a pore-forming cytolysin, and also mVOCs, classified as bitter compounds. The latter are especially effective in triggering massive calcium transients. These observations show that bacterial metabolites can activate CSF-cNs, indicating that they may contribute to the response of sensory neurons we observed *in vivo*.

CSF-cNs selectively express taste receptors and numerous peptides involved in innate immunity

To determine how CSF-cNs could respond to pneumococci, we analyzed CSF-cN-enriched transcripts (Figure 4). The spinal cord of 3 dpf larvae contains approximately 150 CSF-cNs (see cell counts in the transgenic line *Tg(pkd2l1:GFP)* that are all

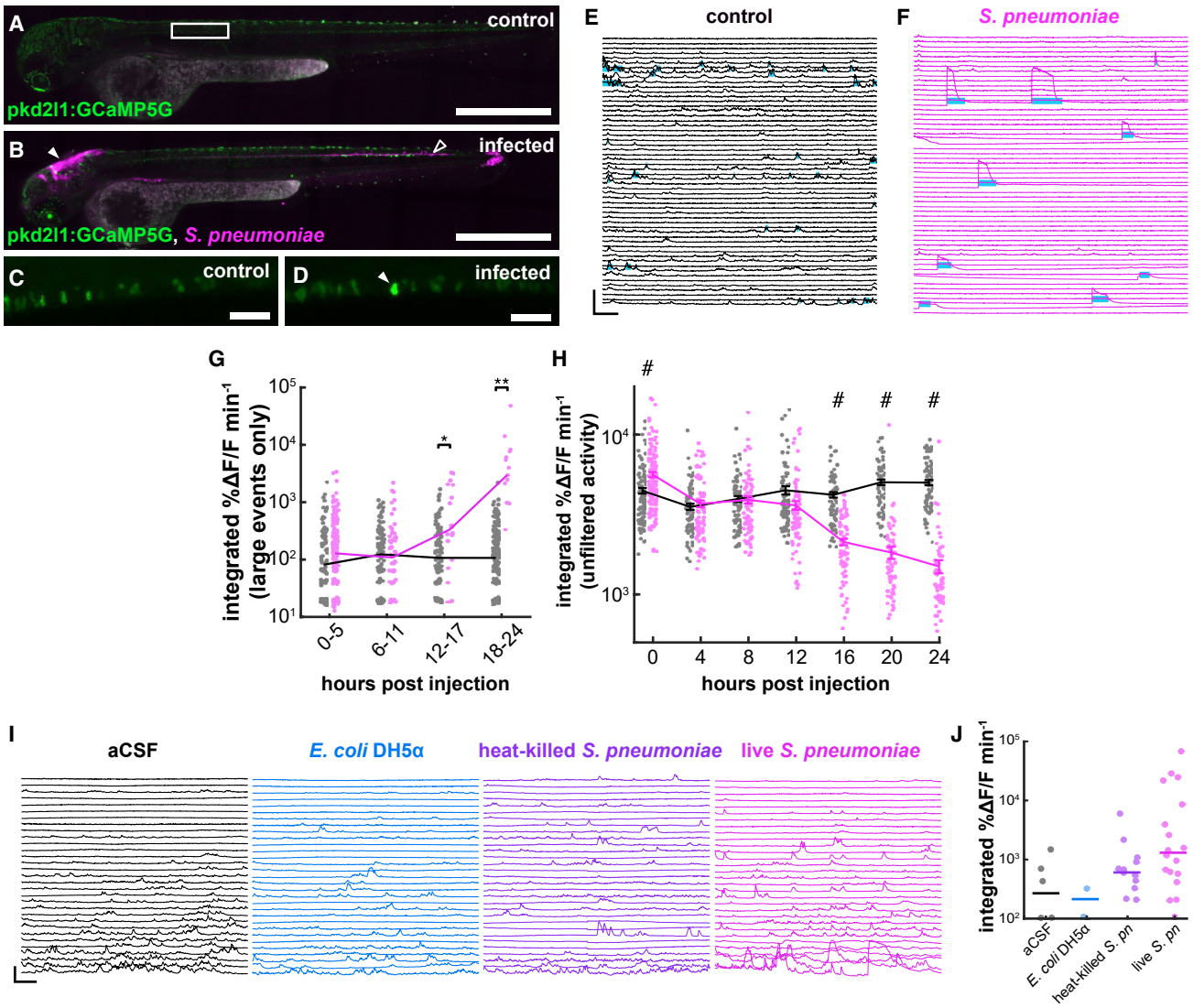

Figure 2. Activity of CSF-cNs drastically changes in response to the invasion of *Streptococcus pneumoniae* into the CSF

(A) Untreated 3 dpf *Tg(pkd2l1:GCaMP5G)* larva. Box indicates field of view for (C) and (D). Scale bars, 500 μm.

(B) Sibling larva, 24 hpi of fluorescently labeled *S. pneumoniae* into the hindbrain ventricle (HBV, indicated by filled arrowhead); empty arrowhead indicates extent of bacterial proliferation.

(C) Higher magnification image of control CSF-cN calcium imaging. Scale bars, 50 μm.

(D) Comparable image from an infected larva with *S. pneumoniae*. Arrowhead indicates a CSF-cN undergoing a high-amplitude transient.

(E) Ca^{2+} activity plots of uninfected CSF-cNs 21 h after the beginning of the experiment. Cyan bars indicate detected long-lasting high-amplitude events. Vertical scale, 500% ΔF/F; horizontal scale, 20 s. These events precede the arrival of neutrophils (Figure S1).

(F) Similar plots from CSF-cNs of infected larvae showing high-amplitude transients.

(G) Quantification of software-detected high-amplitude transients in control (gray) and *S. pneumoniae*-infected (magenta) larvae. Large transients appear 12 hpi (lines represent median values, Wilcoxon signed-rank test, *p < 0.0125, **p < 0.0063).

(H) Integrated Ca^{2+} activity in CSF-cNs in control (gray) and infected (magenta) larvae over 24 h of infection. Overall activity undergoes a decline over the course of infection (two-factor ANOVA, injection factor F = 124.36, p = 1.61 × 10^{-27}, Scheffé post hoc testing, #p < 0.05, data are represented as mean ± SEM).

(I) Individual CSF-cN Ca^{2+} traces from 2 dpf zebrafish injected with aCSF, DH5α *Escherichia coli*, heat-killed *S. pneumoniae*, and live *S. pneumoniae*. Injection with live *S. pneumoniae* elicits by far the largest transients. Vertical scale, 200% ΔF/F; horizontal scale, 25 s.

(J) Quantification of software-detected large transients from the four conditions in (M); lines represent median values. More transients are observed in live infected fish than the other three conditions (chi-square test, p = 6.28E−16).

See also Figure S1, Table S1, and Video S1.

GFP positive; Figure S3). We therefore used fluorescence-activated cell sorting (FACS) to isolate GFP-positive CSF-cNs from guillotined 3 dpf *Tg(pkd2l1:GAL4; UAS:GFP)* larvae[9] (Figures 4A–4C; STAR Methods). Relative to the GFP-negative fraction, the GFP-positive fraction displayed elevated expression of known CSF-cN markers, such as *pkd2l1*,[20,21]

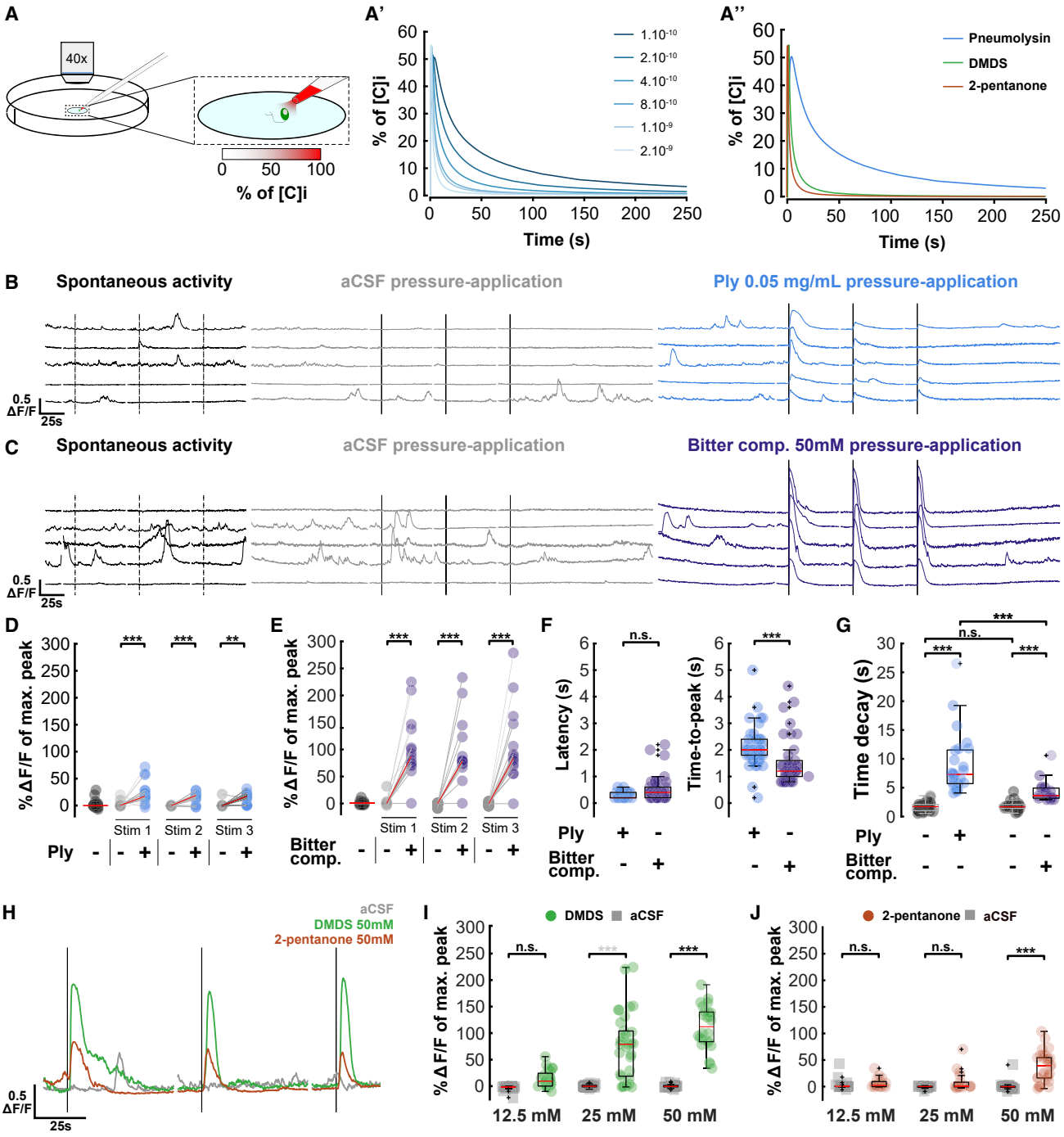

Figure 3. CSF-cNs respond *in vitro* to pneumolysin and bitter compounds

(A) Simulations of *in vitro* CSF-cN stimulation. (A) Schematic view of the *in vitro* stimulation experimental setup combining calcium imaging at 40×, 5 Hz and stimulation of CSF-cN with a gradient of molecule. (A′) Simulation of the concentration of molecule sensed by CSF-cN for a range of coefficients of diffusion (from 1×10^{-10} to 2×10^{-9} m^2/s); [C]i corresponds to initial concentration in the stimulation pipette. (A″) Simulation of the concentration of pneumolysin (Ply), dimethyl disulfide (DMDS), and 2-pentanone; coefficients of diffusion: 1×10^{-10}, 1×10^{-9}, and 2×10^{-9} m^2/s, respectively; [C]i corresponds to initial concentration within the stimulation pipette.

(B) Representative individual *in vitro* CSF-cN Ca^{2+} traces from no stimulation control (left, dark), 3 successive 1-s stimulations of aCSF (middle, gray), and 3 successive 1-s stimulations of 0.05 mg/mL pneumolysin (Ply) (right, blue). Dark lines correspond to 1-s stimulations, and dashed lines correspond to putative 1-s stimulations during spontaneous activity. Vertical scale, 0.5 ΔF/F; horizontal scale, 25 s.

(C) Representative individual *in vitro* CSF-cN Ca^{2+} traces from no stimulation control (left, dark), 3 successive 1-s stimulations of aCSF (middle, gray), and 3 successive 1-s stimulations of 50 mM bitter compounds mix (right, purple). Bitter compound mix: acetone, 2-butanone, 2-pentanone, 2-methylpropanal, and

(legend continued on next page)

pkd1l2,[42,43] and the GABAergic neuronal marker *gad67*, but as expected, no hindbrain-specific markers (*raraa* and *rarab*) (Figure S4).

We then performed RNA-seq on 5 biological replicates and identified 202 transcripts that were enriched in GFP-positive CSF-cNs relative to GFP-negative cells (Figures 4D and 4E; Data S1; STAR Methods). This set contained all previously identified CSF-cN-specific transcription factors for differentiation (members of the *nkx* and *gata* family, *tal2*, and *olig2*),[43–47] enzymes involved in GABA synthesis (*gad65/67*),[20] the transient receptor potential channel *pkd2l1* and associated protein *pkd1l2*,[20,21,42,43] the secreted peptides involved in dorsal arching of the spine (*urp1* and *urp2*),[12,14,15] and the somatostatin *sst1.1*.[48–50]

To validate our CSF-cN transcriptome, we combined fluorescence *in situ* hybridization (FISH) with GFP antibody staining in 1 and 3 dpf *Tg(pkd2l1:GCaMP5G)* transgenic larvae for 47 of the enriched transcripts and found 40 (85%) where gene expression was confirmed and selective to CSF-cNs (Figures 4F–4J″ and S5). The 7 out of 47 genes whose expression was not confirmed corresponded to genes expressed at low level or to contamination from floor plate or motor neurons (the close disposition of the latter can be seen in Figure 4G). In agreement with CSF-cN responses to mVOCs *in vitro* (Figures 3C–3E), orphan taste receptors from the type 2 taste receptor family responding to bitter compounds, *tas2r3a* and *tas2r3b*, were the most enriched transcripts in CSF-cNs (Figures 4D and 4E). We generated a double-knockout zebrafish mutant for the taste 2 receptors *tas2r3a* and *tas2r3b* (Figures S6A–S6C). The calcium response of CSF-cNs to the bitter compound DMDS in these double-knockout mutants was not abolished (Figure S6D), possibly due to compensation by other taste receptors expressed in CSF-cNs that may occur.

The entry of *S. pneumoniae* in the brain triggers host cells to secrete proinflammatory cytokines (such as TNF-α, IL-1, and IL-6) and chemokines (such as monocyte chemoattractant protein-1, macrophage inflammatory protein-1α, and IL-8). Interestingly, we found that CSF-cNs express several immune-related receptors, including the TNF-α receptor (*tnfrsf1a*), IL-13 receptor, and IL-17 receptor (Figure 4E), and several inflammasome components (*asc*, *caspa/b*, and *nod1/2*).

In the category of secreted peptides and proteins, CSF-cNs expressed, in addition to the well-known somatostatin 1.1[49] and urotensin-related peptides,[14] numerous secreted factors implicated in immune responses: *esm1*, *nppc*, *msmp2*, *scg2a*, *sst3*, *ntn1b*, and *txn* (Figures 4G and 4H), some of which were expressed into adulthood (Figures 4I and 4J″).

CSF-cNs upregulate transcripts for secreted factors involved in innate immunity during pneumococcal infection

To investigate changes in CSF-cN expression upon infection, we used FACS again to isolate GFP-positive CSF-cNs from *Tg(pkd2l1:GAL4; UAS:GFP)* larvae and performed RNA-seq on sorted CSF-cNs at 24 hpi of either vehicle or *S. pneumoniae* (Figure 5; STAR Methods). We validated that transcripts (*pkd2l1* and *pkd1l2*) previously found to be CSF-cN specific were again

dimethyl disulfide (DMDS). Dark lines correspond to 1-s stimulations, and dashed lines correspond to putative 1-s stimulations during spontaneous activity. Vertical scale, 0.5 ΔF/F; horizontal scale, 25 s.

(D) Quantification of calcium transients' amplitude elicited by pneumolysin pressure application. Paired line plots showing responses of individual cells to absence of stimulation (corresponding to spontaneous activity, on the left in black circle) or 3 successive 1-s stimuli of aCSF (gray circle) versus 0.05 mg/mL pneumolysin (Ply, blue circle). Two-factor ANOVA, treatment factor $F = 66.185$, $p = 1.47 \times 10^{-12}$, Tukey HSD post hoc testing, ***$p < 0.001$. Red bar: median ΔF/F (median spontaneous activity = 0.03%; median Ply = 17.49% and median aCSF = 0.19% for stimulation 1; median Ply = 18.78% and median aCSF = 0.03% for stimulation 2; median Ply = 17.20% and median aCSF = −0.20% for stimulation 3), 16 responding cells out of 17.

(E) Quantification of the amplitude and kinematics of calcium transients elicited by pressure application of bitter compounds. Paired line plots showing responses of individual cells to absence of stimulation (corresponding to spontaneous activity, on the left in black circle) or 3 successive 1-s stimuli of aCSF (gray circle) versus 50 mM bitter compounds mix (purple circle). Two-factor ANOVA, treatment factor $F = 116.762$, $p < 2.0 \times 10^{-16}$, Tukey HSD post hoc testing, ***$p < 0.001$. Red bar: median ΔF/F (median spontaneous activity = 0.10%; median bitter compounds = 87.26% and median aCSF = 0.05% for stimulation 1; median bitter compounds = 78.85% and median aCSF = −0.13% for stimulation 2; median bitter compounds = 83.64% and median aCSF = −0.50% for stimulation 3), 15 responding cells out of 15.

(F) Quantification of latency and time-to-peak after pneumolysin (blue circle) or bitter compounds in mix (purple circle) stimuli. Red bar: median (for latency, median Ply = 0.2 s and median bitter compounds = 0.4 s, $p > 0.05$; for time-to-peak, median Ply = 2 s and median bitter compounds = 1.2 s, $p < 1 \times 10^{-6}$; Kolmogorov-Smirnov test). Boxplot represents IQR ± minimum/maximum sans outliers.

(G) Quantification of time decay for spontaneous activity (black circle) or after pneumolysin (blue circle) or bitter compounds in mix (purple circle) stimuli. Red bar: median (on the left, median Ply = 7.36 s and median spontaneous activity = 1.71 s, $p < 1 \times 10^{-11}$; on the right, median bitter compounds = 3.59 s and median spontaneous activity = 1.69 s, $p < 1 \times 10^{-6}$, Ply and bitter compounds decays are different, $p < 1 \times 10^{-4}$; Kolmogorov-Smirnov test). Boxplot represents IQR ± minimum/maximum sans outliers. Longer time decay for Ply compared with bitter compounds in mix is probably due to a smaller coefficient of diffusion as shown in (A″).

(H) Illustration of calcium transients after pressure application of DMDS and 2-pentanone. Representative individual *in vitro* CSF-cN Ca^{2+} traces from 3 successive 1-s stimulations with either aCSF (gray), DMDS 50 mM (green), or 2-pentanone 50 mM (brown). Dark lines correspond to 1-s stimulations. Vertical scale, 0.5 ΔF/F; horizontal scale, 25 s.

(I) Quantification of calcium transients after aCSF (gray circle) or DMDS (green circle) stimuli. Two-factor ANOVA, treatment factor $F = 170.58$, $p \leq 2.0 \times 10^{-16}$, concentration factor $F = 29.43$, $p = 1.66 \times 10^{-11}$, Tukey HSD post hoc testing, ***$p < 0.001$, n.s., not significant. Red bar: median ΔF/F (median 12.5 mM DMDS = 9.44% and median aCSF = −1.20%, 6 responding cells out of 8; median 25 mM DMDS = 78.96% and median aCSF = −0.26%, 8 responding cells out of 10; median 50 mM DMDS = 112.09% and median aCSF = −0.54%, 8 responding cells out of 8). Boxplot represents IQR ± minimum/maximum sans outliers.

(J) Quantification of calcium transients after aCSF (gray circle) or 2-pentanone (brown circle) stimuli. Two-factor ANOVA, treatment factor $F = 53.48$, $p = 2.67 \times 10^{-11}$, concentration factor $F = 13.89$, $p = 3.53 \times 10^{-6}$, Tukey HSD post hoc testing, ***$p < 0.001$, n.s., not significant. Red bar: median ΔF/F (median 12.5 mM 2-pentanone = 2.19% and median aCSF = 0.14%, 4 responding cells out of 6; median 25 mM DMDS = 0.63% and median aCSF = 0.04%, 3 responding cells out of 6; median 50 mM DMDS = 39.72% and median aCSF = −0.39%, 9 responding cells out of 10). Boxplot represents IQR ± minimum/maximum sans outliers. Figure S2 shows similar results for bitter compounds that do not activate CSF-cNs, suggesting some specificity.

See also Figure S2 and Video S2.

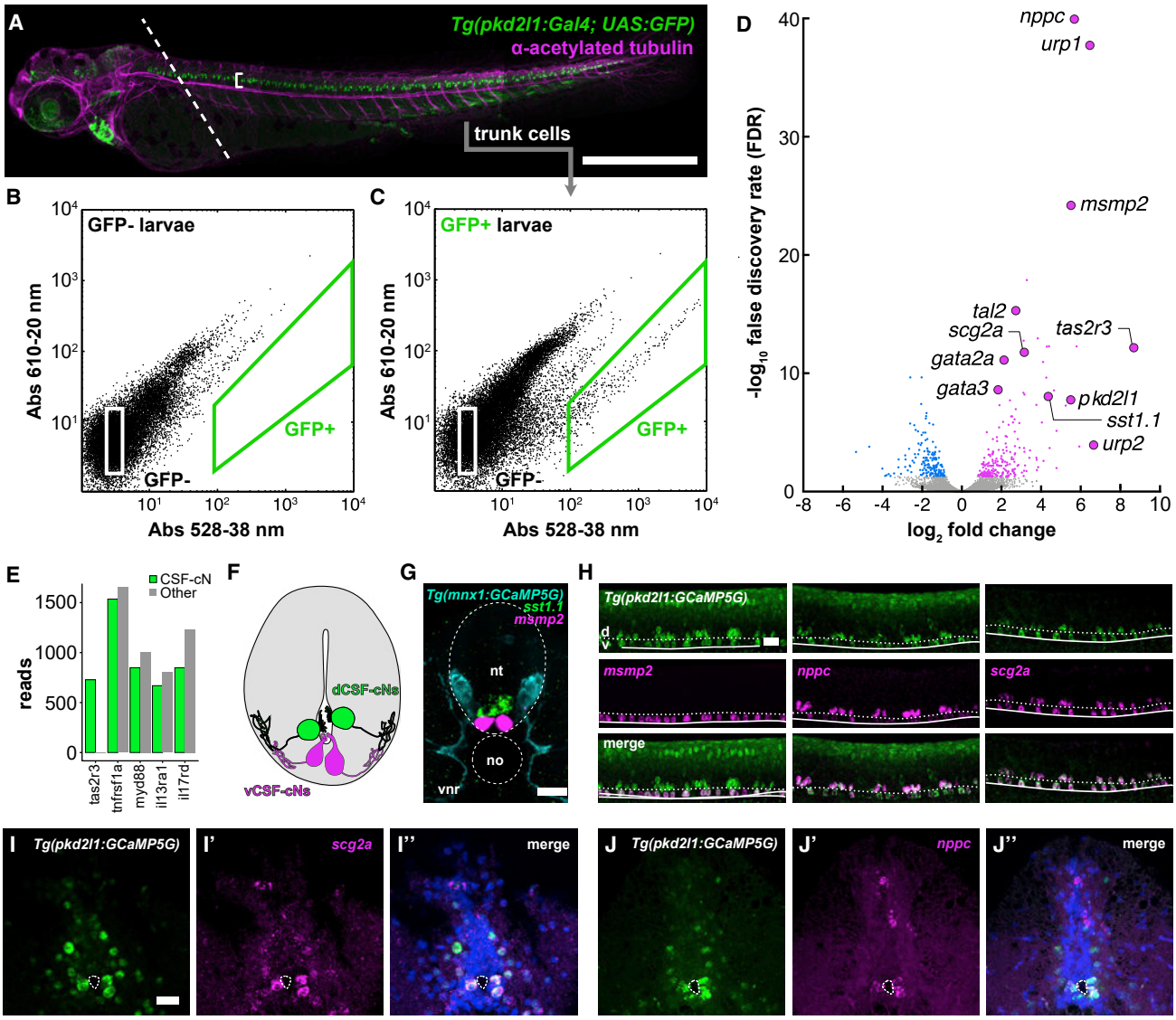

Figure 4. The CSF-cN transcriptome reveals the expression of taste receptors and immune-related secreted factors

(A) 3 dpf zebrafish *Tg(pkd2l1:GAL4; UAS:GFP)* larva immunostained for GFP (green) and acetylated tubulin (magenta). Dashed line indicates plane of decapitation prior to dissociation (anterior tissues were discarded to exclude labeled cells in brain and heart); bracket indicates CSF-cN domain. Scale bars, 500 μm.

(B) Calibration FACS plot from non-transgenic siblings.

(C) FACS plot from a typical dissociation of cells from transgenic larvae. A small fraction (~0.2% of input) of cells is green-shifted. Figure S3 quantifies the upper bound of cells/larvae we could reasonably expect to obtain. In Figure S4A, we use qPCR to show that this fraction appeared to be CSF-cNs.

(D) Volcano plot of all RNA-seq replicates: 202 transcripts were enriched in CSF-cNs. Figure S4B provides more categorical information on these hits. Figure S6 shows that knocking out individual CSF-cN-enriched taste receptors identified by this approach did not impair CSF-cNs' ability to detect bitter compounds.

(E) Quantification of reads for selected immune-related receptors in both GFP^+ CSF-cNs and GFP^- (i.e., all other) cells.

(F) Schematic representation of a transverse section of the spinal cord and central canal showing the disposition of dorsolateral CSF-cNs (dCSF-cNs, green) and ventromedial CSF-cNs (vCSF-cNs, magenta).

(G) A mixed fluorescence *in situ* hybridization/immunofluorescent stain showing the disposition of motor neurons (cyan, *Tg(mnx1:GCaMP5)*), dCSF-cNs (green, *sst1.1*), and vCSF-cNs (magenta, *msmp2*). The section here is a frontal section, e.g., a cross-section of the spinal cord. Scale bars, 50 μm.

(H) Fluorescence *in situ* hybridization reveals that the putative immune-related secreted factors *msmp2*, *nppc*, and *scg2a* are expressed in CSF-cNs. These confocal stacks are lateral stacks, so at 90° orientation to the image in (G). Scale bars, 50 μm. Figure S5 shows additional *in situ* hybridization results from some of these RNA-seq hits; most hits we assessed were verified histologically.

(I) Transverse section of adult *Tg(pkd2l1:GCaMP5G)* spinal cord; expression of *scg2a* is specific to CSF-cNs. Scale bars, 50 μm.

(J) Adults continue to express *nppc* and *scg2a* in CSF-cNs.

See also Figures S3–S6, Table S1, and Data S1.

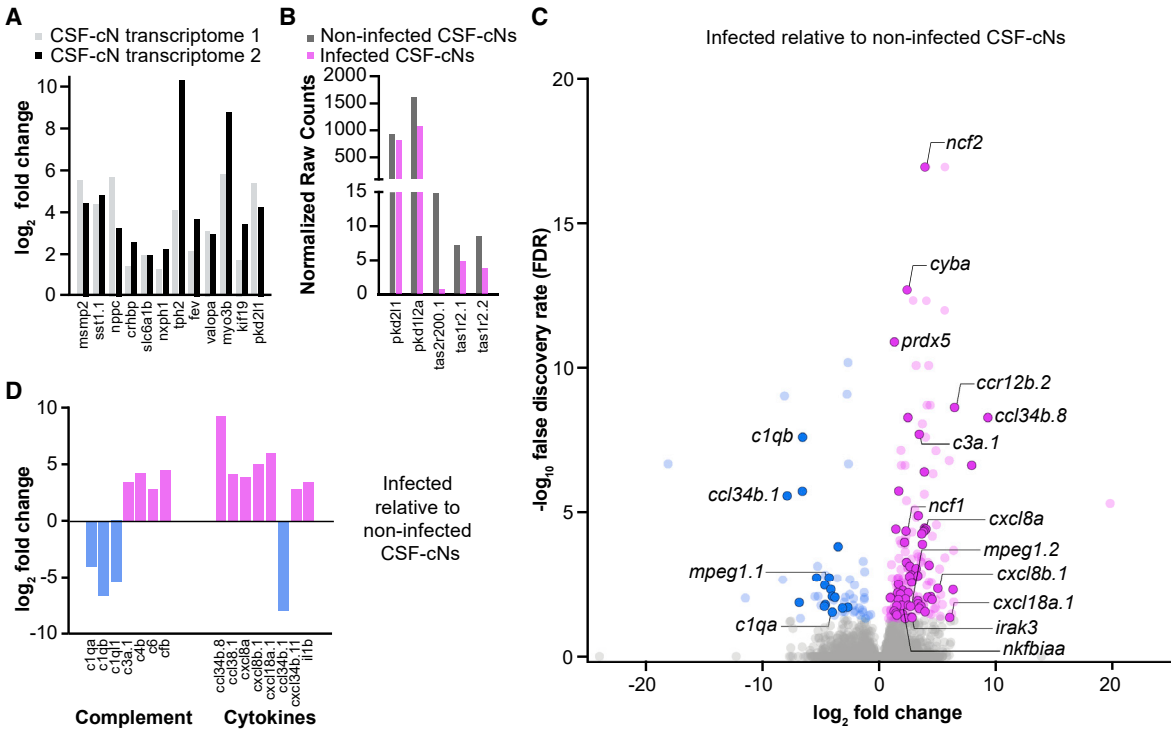

Figure 5. RNA-seq shows upregulation of complement system of the alternative and terminal pathway as well as cytokines in CSF-cNs during *S. pneumoniae* infection

(A) Log fold change bar plot comparing enrichment of known CSF-cN transcripts in the GFP$^+$ fraction with control GFP$^-$ cells in the original differential transcriptome 1 (gray bars; see Figure 4 and Table S1) and subsequent transcriptome 2 for non-infected larvae (black bars; see Table S1).

(B) A plot of raw reads comparing selected receptors in non-infected (gray bars) and infected (pink bars) CSF-cNs, showing that the expression of receptors that are specifically enriched in CSF-cNs (*pkd2l1*, *pkd1l2*, and taste receptors) remains stable.

(C) Volcano plot comparing the expression of transcripts in infected CSF-cNs relative to uninfected CSF-cNs. Transcripts for several immune-related secretory compounds are differentially expressed.

(D) Log fold change bar plot of selected immune-related transcripts corresponding to complement system and cytokines from the same data as in (B). We observe significant upregulation of complement system of the alternative (C3), classical (C4), and terminal (C6) pathway (left side) as well as cytokines (right side).

See also Table S1 and Data S1.

enriched in this dataset, and we found numerous taste 1 and 2 receptor families such as *tas2r200.1*, *tas1r2.2*, and *tas1r2.1* (Figure 5A; Data S1), while transcripts for receptors (*pkd2l1*, *pkd1l2*, *tas1r2.1*, *tas2r200.1*, and *tas1r2.2*) did not increase upon infection in CSF-cNs (Figure 5B). By contrast, numerous transcripts encoding immune-related secretory compounds were upregulated in CSF-cNs upon infection (76 out of 231, 33%; Figures 5C and 5D; Data S1): multiple cytokines including IL-1β and IL-8/CXCL8 (Figure 5D, right), and complement factors C3 (alternative pathway), C4 (classical and lectin pathway), and C6 (terminal pathway) (Figure 5D, left).

Secretion from CSF-cNs contributes to host defense during pneumococcal infection

To test the role of CSF-cNs in host defense, we ablated CSF-cNs at 2 dpf using the nitroreductase/metronidazole (MTZ) chemogenetic system (Figures 6A, 6B, 6D, and S3)[51] or selectively blocked their secretion using the botulinum toxin B light chain fused to GFP (BoTxBLC-GFP; Figures 6C, 6E, and 6F).[52] After MTZ treatment (Figures 6A and 6B), nitroreductase-expressing and non-expressing larvae were infected the following day and scored for survival every 12 h. We observed that MTZ itself conferred a survival benefit in control fish (38% survival 96 hpi; Figure 6D). Larvae in which CSF-cNs were ablated, however, exhibited a nearly 3-fold decrease in survival (13% survival 96 hpi; Figure 6D).

As large and sustained calcium transients, observed in CSF-cNs during pneumococcal infection (Figure 2), enable the SNARE-dependent docking and releasing of dense core vesicles containing peptides,[53–56] we next tested the role of SNARE-dependent neurosecretion from CSF-cNs during infection. By cleaving VAMP2,[57] we previously showed that the expression of BoTxBLC effectively prevents vesicular fusion and release in CSF-cNs.[52] In *Tg(pkd2l1:GAL4; UAS:BoTxBLC-GFP)* transgenic larvae in which BoTxBLC was selectively expressed in CSF-cNs (Figure 6C),[52] the survival following infection at 2 dpf was reduced by 2-fold, compared with their control siblings (15% compared with 32% survival at 96 hpi; Figure 6E). Accordingly, more live bacteria were observed 24 h after infection in transgenic larvae in which CSF-cN neurosecretion was altered, compared with control siblings (Figure 6F). In order to test whether individual CSF-cN peptides were involved in this effect, we generated zebrafish knockout mutants for the peptides *scg2a*, *nppc*, and *esm1* found specifically in CSF-cNs in the trunk. None of the individual homozygous

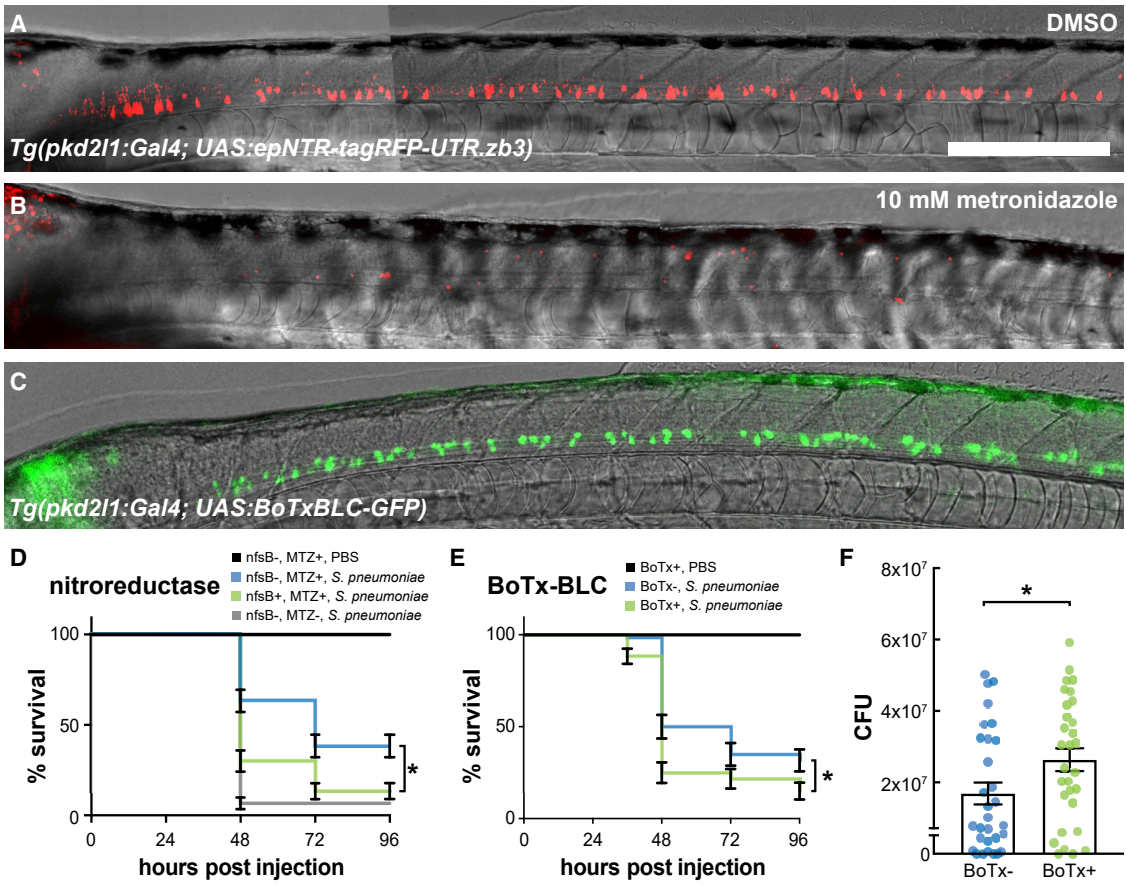

Figure 6. Secretory activity of CSF-cNs confers a survival benefit during pneumococcal meningitis

(A) *Tg(pkd2l1:GAL4; UAS:epNTR-tagRFPT-UTR.zb3)* larva at 3 dpf following 24 h of incubation in 0.1% DMSO. Scale bars, 500 μm. Figure S3 addresses how complete NTR expression is in the full complement of CSF-cNs.

(B) Sibling larva incubated for the same time period in 10 mM metronidazole (MTZ). All tagRFP$^+$ CSF-cNs are lost.

(C) Expression of BoTxBLC-GFP in the *Tg(pkd2l1:GAL4; UAS:BoTxBLC-GFP)* larva at 3 dpf.

(D) Survival curves of *Tg(pkd2l1:GAL4; UAS:epNTR-tagRFPT-UTR.zb3)*(nfsB) larvae and their siblings when exposed to metronidazole or DMSO from 1 to 2 dpf, washed with fish facility water, and subsequently infected with 4,000 CFU *S. pneumoniae*. Metronidazole alone slightly protects larvae against infection by *S. pneumoniae* (compare blue and gray lines, log-rank test, $p < 0.0001$). However, metronidazole-mediated ablation of CSF-cNs confers a large survival deficit (compare blue and green lines, log-rank test, $p = 0.0002$). The survival data represent the mean ± SEM of three individual experiments with n = 20 larvae per group (total n = 60 per group).

(E) Survival curves of *Tg(pkd2l1:GAL4; UAS:BoTxBLC-GFP)* ("BoTx") larvae (green line) and non-transgenic sibling controls (blue line) injected with ~300 CFU *S. pneumoniae* D39 wild-type strain into the hindbrain ventricle at 2 dpf reveal that BoTx-expressing larvae exhibit higher mortality rates (log-rank test, $p = 0.0065$). The survival data represent the mean ± SEM of three individual experiments with n = 20 larvae per group (total n = 60 per group). Figure S7 shows that knocking out individual secreted factors identified by the transcriptome does not impair larval survival in the meningitis model.

(F) *Tg(pkd2l1:GAL4; UAS:BoTxBLC-GFP)* (referred to as "BoTx") larvae (green line) exhibit higher bacterial loads at 24 h post injection as compared with non-transgenic sibling controls (unpaired t test, $p = 0.0368$). Each dot represents a single larva. Error bars = mean ± SEM of three individual experiments with n = 10 larvae per group (total n = 30 per group).

See also Figures S3 and S7 and Table S1.

mutants statistically differed in terms of survival, compared with their control siblings (Figure S7), suggesting that multiple secretory compounds act in concert. Altogether, our results indicate that CSF-cNs contribute to host survival in response to pneumococcal meningitis via VAMP2-dependant extracellular secretion, likely via the release of multiple secreted factors.

CSF-cNs respond to multiple types of pathogens

To test whether CSF-cNs respond to other pathogen-related cues, we tested CSF-cN response to supernatant of *S. pneumoniae*, to culture medium from cells infected with a neurotropic virus (Sindbis virus; SINV), as well as to another Gram-positive bacterium that is known to cause meningitis, *Listeria monocytogenes* (Figure 7). *S. pneumoniae* supernatant elicited large calcium responses in CSF-cNs *in vitro* (73.35% on average observed in all cells tested, n = 6; Figures 7A and 7B). Similarly, the UV-inactivated supernatant of cells infected with SINV elicited large calcium transients in CSF-cNs *in vitro* that were not observed in the control supernatant (45.63% on average observed in all cells tested, n = 7; Figures 7C and 7D). Finally, we tested the response of CSF-cNs to *L. monocytogenes in vivo* using the same injection paradigm

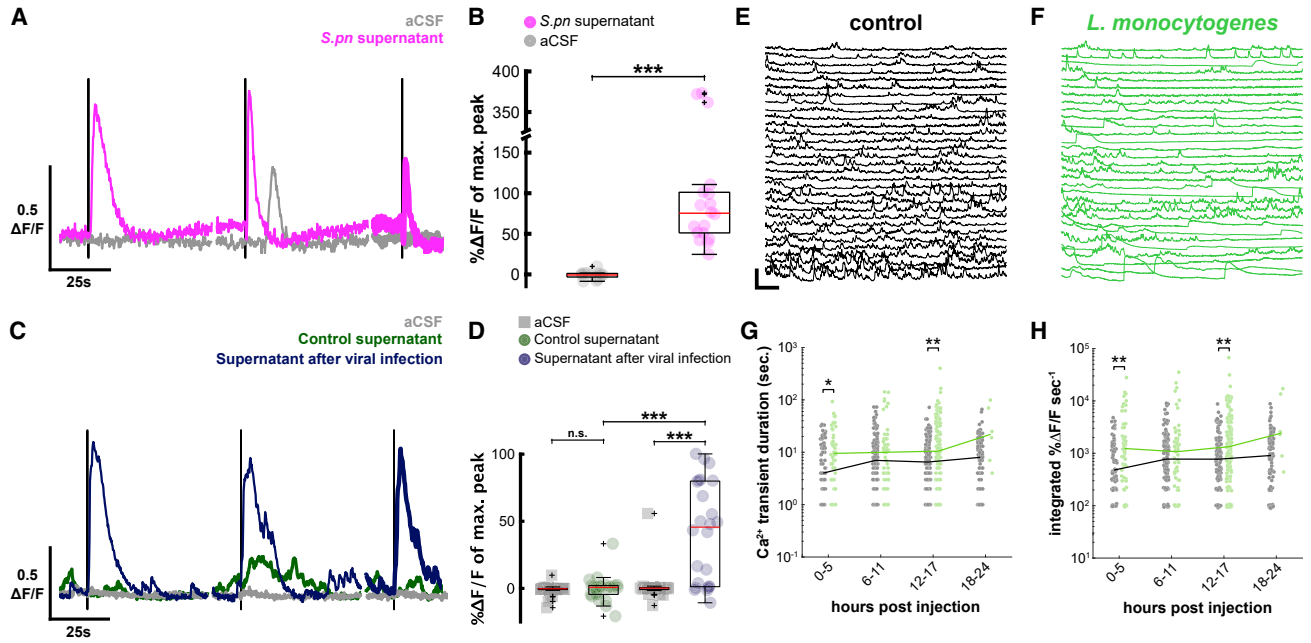

Figure 7. *Streptococcus pneumoniae* supernatant, virus culture supernatant, and *Listeria monocytogenes* infection also activate CSF-cNs

(A) Representative individual *in vitro* CSF-cN Ca^{2+} traces from 3 successive 1-s stimulations of aCSF (gray) and supernatant (purple). Dark lines correspond to 1-s stimulations. Vertical scale, 0.5 ΔF/F; horizontal scale, 25 s.

(B) Quantification of calcium transients after aCSF (gray circle) or *S. pneumoniae* supernatant (purple circle) stimuli. Paired t test, $p = 5.0 \times 10^{-4}$, ***$p < 0.001$. Red bar: median ΔF/F (median *S. pneumoniae* supernatant = +75.35% versus median aCSF = −0.73%, n = 6 cells). Boxplot represents IQR + minimum/maximum sans outliers.

(C) Representative individual *in vitro* CSF-cN Ca^{2+} traces from 3 successive 1-s stimulations of aCSF (gray), UV-inactivated supernatant of BHK cells infected with Sindbis virus (blue), and control BHK supernatant (green). Dark lines correspond to 1-s stimulations. Vertical scale, 0.5 ΔF/F; horizontal scale, 25 s.

(D) Quantification of calcium transients after aCSF (gray circle), control supernatant (green circle), or supernatant after viral infection (blue) stimuli. Two-factor ANOVA, treatment factor F = 24.52, $p = 3.32 \times 10^{-6}$, Tukey HSD post hoc testing, ***$p < 0.001$. Red bar: median ΔF/F (median control supernatant = +0.82% versus median aCSF = −0.26%, n = 8 cells; median supernatant after virus infection = 45.63% versus median SF = −0.22%, n = 7 cells; median 100 mM DMDS = 112.09% versus median aCSF = −0.54%, n = 8 cells.

(E) *In vivo* Ca^{2+} activity of CSF-cNs in uninfected larvae 8 h after injection in the brain ventricle. Vertical scale, 250% ΔF/F; horizontal scale, 20 s.

(F) Long-lasting and large calcium transients from larvae infected with *L. monocytogenes* occur in a similar manner as with *S. pneumoniae*.

(G) Quantification of duration of software-detected high-amplitude transients in control (gray) and *L. monocytogenes*-infected (green) larvae (Wilcoxon signed-rank test, *$p < 0.0125$, **$p < 0.0063$). Lines indicate median values.

(H) Similar quantification of integrated signal of large transients during *L. monocytogenes* infection.

See also Table S1.

as with *S. pneumoniae* (Figures 7E–7H). Our results suggest that CSF-cNs not only respond to live *S. pneumoniae* but also to their by-products secreted upon infection, as well as other bacteria and viruses.

DISCUSSION

Pathogenetic steps of pneumococcal meningitis involve mucosal colonization and invasion, survival, and replication in the bloodstream, followed by traversal of the blood brain/CSF barrier.[26] How the initial host immune response is orchestrated in the phase of bacterial penetration in the CSF remains incompletely understood. In a meningitis model in larval zebrafish, we show here that central sensory neurons respond to the invasion of *S. pneumoniae* dividing in the CSF and that neurosecretion from these neurons contributes to host survival. The timing of this response suggests that the phenomena we report on in the spinal cord do not likely relate to the earliest steps of detection of pathogens in the CNS but to later stages that nonetheless precede changes in muscle tonus. Owing to the role of CSF-cN peptides in triggering dorsal arching, we emphasize as well that CSF-cN activation may instead explain the evolution of symptoms at the advanced stage of meningitis, including the hallmark stiffness of the neck and opisthotonos.

Response to pathogenic bacteria proliferating in the CSF

We tested whether CSF-cNs could be directly or indirectly activated by chemical cues secreted by pathogenic bacteria during growth. As we did not observe an activation of ependymal radial glial cells—the most prominent CSF-contacting cell type along the central canal—during the *S. pneumoniae* infection, we hypothesized that bacterial products could trigger a response in CSF-cNs. To support this hypothesis, we found that CSF-cNs selectively express orphan taste 2 receptors for bitter compounds. We further demonstrated *in vitro* that CSF-cNs exhibit calcium transients in response to microbial metabolites acting as bitter compounds and to pneumolysin, a cytolysin and major

virulence factor released by pneumococci during growth. The CSF-cN response to bitter compounds was stronger than that to pneumolysin. These observations suggest that bacterial metabolites could directly trigger the response of sensory neurons we observed *in vivo*. Remarkably, the response to pathogenic bacteria as long and massive calcium transients occurs in a subset of CSF-cNs, possibly due to local changes in the growth and structures formed by bacteria. While dorsal arching appears at least 24 hpi, these transients occur in fully paralyzed, agarose immobilized fish well before 24 hpi, indicating that CSF-cN activation precedes the start of spinal curvature. CSF-cN calcium transients do not originate from pre-apoptotic calcium phenomenon, as they recur in individual cells over many hours without apparent cell death. *In vivo*, heat-killed bacteria and non-virulent bacteria failed to elicit as strong a response as we observed during live infection, suggesting that metabolites released by live bacteria proliferating in the CSF, or proinflammatory cues from host cells infected by the pathogenic bacteria, are necessary to activate CSF-cNs. Secretion of bitter compounds by bacteria has been shown to activate chemosensory neurons in the lung epithelium via type 2 taste receptors.[35–37,39,40,58,59] We show here that similarly at least two of these bitter compounds, DMDS and 2-pentanone, known to be secreted by *S. pneumoniae*,[40,41] strongly activate CSF-cNs in primary cultures. DMDS is also known to be secreted by *Neisseria meningitidis*, *Haemophilus influenzae*, and *L. monocytogenes*, after *S. pneumoniae*—the most common causative pathogens of bacterial meningitis.[26,35,58,60]

This initial study begins to address the diversity of pathogens that can cause CNS infection. In addition to responding to pneumococcal infection, we have evidence that CSF-cNs also respond to *L. monocytogenes*, the third most common cause of community-acquired bacterial meningitis.[27] We found that CSF-cNs also responded to the supernatant of cells infected by SINV, a neurotropic virus in zebrafish.[61] Future studies should address mechanisms by which CSF-cNs can respond to such diverse pathogens and further characterize the diversity of pathogens that can activate CSF-cNs.

Promotion of host survival during a bacterial infection of the CNS

During an infection with *S. pneumoniae*, when comparing survival of zebrafish larvae without CSF-cNs with that of their control siblings, CSF-cNs confer a 3-fold survival benefit to the host. We found that the selective blockage of neurosecretion in CSF-cNs led alone to a 2-fold reduction of survival in infected larvae. Accordingly, we found an elevated bacterial load in larvae where neurosecretion had been impaired. Although we did not monitor *in vivo* exocytosis at the CSF-cN membrane in the context of infection, our results from calcium imaging, transcriptome during infection, and survival upon silencing of CSF-cN release are all consistent with a model in which, upon activation, CSF-cNs release compounds that improve survival of the host (see graphical abstract). CSF-cNs can secrete multiple neuropeptides (*somatostatin 1.1*, *secretogranin 2a*, and *nppc*, among others; Figure 4) that they highly express at baseline together with the secreted compounds whose expression we found unregulated during an infection (Data S1), including cytokines and complement factors (Figures 5C and 5D). The mechanisms by which CSF-cNs promote host survival likely involve the secretion of multiple factors, including antimicrobial peptides such as secretogranin 2a[62] or the release of factors modulating inflammatory signaling (*msmp2*, *esm1*, *txn*, *nppc*, *sst3*, and *ntn1b*).[63–70] Knocking out single peptides did not lead to a decrease in survival in our infection model, possibly due to redundancy.[71] Combining knockouts of multiple peptides may be needed to observe an effect on survival rates. Since large calcium transients such as those observed in CSF-cNs during pneumococcal infection are typically necessary for neurosecretory cells to release the content of dense core vesicles in which peptides and secreted proteins are loaded,[53] we speculate that the large transients observed in CSF-cNs during the infection induce secretion. The reduced survival that we observed for zebrafish larvae with impaired CSF-cN secretion supports this hypothesis. Interestingly, an activation of broad neurosecretion in CSF-cNs would lead to an increase in the circulation of peptides of the urotensin family, which recently have been shown to precisely elicit dorsal arching in *Xenopus* and zebrafish embryos and larvae.[12,14–19] By this means, CSF-cN activation during bacterial infection could directly lead to the postural defects referred to as stiffness of the neck and opisthotonos, which are pathognomonic signs for meningeal infection in patients of unknown origin.

Taken together, our data reveal that CSF-cNs can play an important role in CNS defense by tasting the CSF to detect the presence of multiple bacterial and viral pathogens and by secreting factors that enhance the innate immune response. It does, however, have some limitations. First, our observations that pneumolysin and bacterial metabolites elicit calcium transients in CSF-cNs *in vitro* only suggest that these molecules may be involved *in vivo*. Accordingly, CSF-cNs express multiple orphan bitter taste receptors that could mediate the response to bacterial metabolites, but CSF-cN response to bitter compounds was not abolished in double bitter taste receptor mutants for *tas2r3a/b*. Further studies are needed to decipher the contribution of these pathways to CSF-cN response during pneumococcal infection as well as the chemical cues secreted by bacteria *in vivo*. The redundancy of taste receptor expression in CSF-cNs suggests that loss of function of a subset only may not be sufficient to ablate the calcium response to pathogens. Furthermore, we serendipitously identified two likely *tas2r3* paralogs in our fish, but there could be more due to incomplete annotation of the genome.

Second, consistent with an induction of CSF-cN neurosecretion during infection, larval zebrafish exhibited a dorsal arching posture, in a similar manner to that described upon injection of CSF-cN-specific peptides from the urotensin family.[12,14–19] Upon pneumococcal infection of the CNS, we showed that CSF-cNs upregulated the expression of secreted factors (cytokines and complement factors). Together with the evidence that blocking secretion from CSF-cNs reduced host survival and increased bacterial loads, our results point toward an activation of secretion of CSF-cNs during infection to promote innate immunity. We were unable to affect post-infection survival by knocking out any of the expressed secreted factors individually. However, again, any individual loss of function may be insufficiently deleterious as peptides may exhibit redundancy. Future studies will be needed to monitor vesicular fusion associated

with CSF-cN neurosecretion *in vivo*. Third, our results indicate that ciliated sensory neurons in contact with the CSF exhibit categorically different calcium responses to pathogenic bacteria *in vivo*, although they homogeneously responded to pneumolysin and bitter compounds *in vitro*. This discrepancy suggests that the CSF in the central canal is a heterogeneous medium, where pneumococci may differ locally in terms of density or state during an infection. Although estimating the density and movements of bacteria is theoretically possible *in vivo* by using confocal microscopy with mCherry-positive bacteria, monitoring two channels to collect the information of CSF-cN activation does lead to phototoxicity and subsequent silencing of activity in CSF-cNs. This experiment could therefore not be achieved with the fluorescent sensors available for monitoring calcium and bacteria simultaneously *in vivo*. It is critical to note here that the observed calcium transients may not correspond to the earliest steps of detection of pathogens as they occur more than 10 h into infection. CSF-cNs may therefore contribute more to later symptoms (such as opisthotonos and seizures) rather than to initial pathogen detection. We effectively did correlate the loss of CSF-cN function with reduced survival. However, our study did not show the causal link between CSF-cN activation via massive calcium transients and larval survival. As it is well known for other neurosecretory systems, massive calcium transients are associated with exocytosis of dense core vesicles containing peptides. Since blocking neurosecretion specifically in CSF-cNs reduced survival, we propose that CSF-cNs are activated by the presence of bacteria in the CSF and respond by secretion to boost innate immunity. Whether CSF-cN calcium events are necessary to improve survival will be the subject of subsequent studies.

Similarity with peripheral sensory neurons involved in proprioception and pain

CSF-cNs are located in an ideal position to respond to pathogenic bacteria invading the CSF, as well as to modulate immunity in the CNS by interacting with resident microglia and circulating leukocytes recruited in the ventricular space. Our discovery that *in vivo*, central sensory neurons are activated by live pathogens in the CSF and that they confer a survival benefit to the host recalls recent *in vitro* results on peripheral nociceptive sensory neurons activated by bacteria[1,72] or nodose ganglia.[73] Dorsal root ganglia (DRG) are anatomically positioned to detect pathogens entering the body following injury. The similarity in sensory and secretory properties between nociceptive peripheral neurons and interoceptive CSF-cNs is important: (1) DRG, like CSF-cNs, are activated by bacterial toxins as well as other bacterial products,[1] and (2) upon activation, both DRG and CSF-cNs secrete immunomodulatory neuropeptides.[1,72–74] Our results therefore emphasize that sensory neurons are tuned throughout the nervous system (peripheral and central) to respond to intruding pathogens and to promote host survival. We find here that CSF-cNs carry polymodal sensory functions in different physiological contexts. We and others have shown that these neurons are mechanosensory cells activated by spinal compression,[5,8] influencing posture[10,11] and leading to dorsal arching by release of urotensin-related peptides.[12,14,15,52] We show here that CSF-cNs' sensory role can be expanded to tasting chemical compounds in the CSF associated with the intrusion of bacteria, and it provides a potential mechanism by which CSF-cN activation could lead to postural defects that are pathognomonic for meningeal infection.

STAR★METHODS

Detailed methods are provided in the online version of this paper and include the following:

- KEY RESOURCES TABLE
- RESOURCE AVAILABILITY
  - Lead contact
  - Materials availability
  - Data and code availability
- EXPERIMENTAL MODEL AND SUBJECT DETAILS
  - Zebrafish handling and husbandry
  - Bacterial strains and growth conditions
  - Primary cell culture of CSF-cNs
- METHOD DETAILS
  - Confocal imaging
  - Bacterial load
  - Simulations of *in vitro* CSF-cN stimulation
  - Fluorescence activated cell sorting of CSF-cNs and validation
  - Library preparation and RNAseq (differential CSF-cN RNAseq)
  - Fluorescent *in situ* hybridization and immunohistochemistry
  - Generation of transgenic zebrafish lines
  - Generation of *tas2r3* mutants
  - Generation of mutants in genes encoding CSF-cN neuropeptides
  - Calcium imaging of zebrafish larvae after injections in the hindbrain ventricle
  - Calcium imaging in primary cell culture
  - FACS sorting of infected larvae
  - Library preparation and RNAseq (uninfected vs. infected CSF-cNs)
  - RNAseq (uninfected vs. infected CSF-cNs) analysis using DESeq2
  - Larval zebrafish survival assays
  - Survival experiments in CSF-cN compromised transgenic larvae
  - Survival experiments in mutant larvae
  - Analysis of calcium transients *in vivo*
  - Analysis of calcium transients *in vitro*
  - Production of virus-containing supernatant
  - Analysis of neutrophil infiltration to the central canal after infection
  - Behavioral analysis
- QUANTIFICATION AND STATISTICAL ANALYSIS
  - Behavioral analysis
  - Quantification and analysis of axial curvature and fluorescence
  - In vivo calcium imaging
  - RNAseq
  - In vitro calcium imaging
  - Survival analysis

SUPPLEMENTAL INFORMATION

Supplemental information can be found online at https://doi.org/10.1016/j.cub.2023.01.039.

ACKNOWLEDGMENTS

We wish to thank Sophie Nunes-Figueiredo, Antoine Arneau, Monica Dicu, and Bénédicte Daboval for keeping fish in excellent housing conditions in the PhenoZfish facility of the Paris Brain Institute. We thank Prof. Hitoshi Okamoto and Prof. Wilbert Bitter for fruitful discussions; Bethany Berry for her generous gift of *gfap* promoter construct (originally cloned by Brooke Gaynes); Prof. Jan-Willem Veening for providing the *S. pneumoniae* D39 HlpA-mCherry and *S. pneumoniae* D39 HlpA-GFP strains; Dr. Taurai Tasara for providing the *L. monocytogenes* LL195 strain; Yannick Marie, Romain Daveau, and Justine Guégan for their critical assistance in completing the transcriptomic analysis; Dr. Giovanna Barba-Spaeth for her help with UV-inactivation; as well as Cora Chadick, Jeroen Kole, Coen Kuijl, and Theo Verboom for technical assistance. C.W. was a New York Stem Cell Foundation (NYSCF) Robertson Investigator (grant no. NYSCF-R-NI39). This work was supported by the Fondation Schlumberger pour l'Education et la Recherche (FSER/2017), the Fondation pour la Recherche Médicale (FRM no. Equation 202003010612), the ERC Starting Grant "Optoloco" no. 311673, ERC PoC "ZebraZoom" no. 825273, and ERC Consolidator Grant "Exploratome" no. 101002870 (to C.W.). We acknowledge support from "MeninGene" no. 281156 and the HFSP Program grant nos. RGP0063/2014 and RGP0063/2017 and grants from the Agence Nationale de la Recherche (ANR) ASCENTS no. ANR-21-CE13-0008, MOTOMYO no. ANR-21-CE14-0042, and ANR LOCOCONNECT no. ANR-22-CE37-0023 et la Fondation Bettencourt-Schueller don 0031. D.v.d.B. was supported by a ZonMw VICI grant no. 391819627. A.E.P. was supported by an EMBO long-term fellowship (ALTF-549-2013) and a Research in Paris grant from the Marie de Paris. L. Desban was supported by the French Ministry of Higher Education and Research doctoral fellowship. M.D. was supported by a PhD fellowship from the Sorbonne Université Ecole Doctorale ED3C.

AUTHOR CONTRIBUTIONS

The project was conceived by C.W., C.M.J.E.V.-G., A.E.P., K.K.J., and D.v.d.B. A.E.P., L. Desban, and K.K.J. performed FACS and transcriptome analysis with the help of F.-X.L. for statistical analysis. A.E.P., K.K.J., and C.W. combined bacterial infections with calcium imaging. H.M. performed primary culture experiments and collected all calcium imaging data *in vitro*. A.E.P., K.K.J., H.M., A.H., F.B.Q., and C.W. performed the behavioral experiments and postural analysis. A.E.P., H.M., F.B.Q., L. Desban, and L. Djenoune performed histochemistry and provided *in situ* gene expression data. V.L. and J.-P.L. produced the SINV supernatants. M.D. counted CSF-cNs for supplemental figure. J.-P.L. and P.-L.B. provided advice on the transcriptome analysis. J.R. helped with Tol-mediated transgenesis for one fish transgenic line. A.E.P., K.K.J., and F.B.Q. performed survival analysis. C.W., A.E.P., K.K.J., H.M., and F.B.Q. generated figures. C.W., A.E.P., K.K.J., C.M.J.E.V.-G., and D.v.d.B. wrote the manuscript with input from all authors.

DECLARATION OF INTERESTS

The authors declare no competing interests.

INCLUSION AND DIVERSITY

We support inclusive, diverse, and equitable conduct of research.

Received: July 25, 2022
Revised: December 8, 2022
Accepted: January 19, 2023
Published: February 14, 2023

REFERENCES

1. Chiu, I.M., Heesters, B.A., Ghasemlou, N., Hehn, C.A.v., Zhao, F., Tran, J., Wainger, B., Strominger, A., Muralidharan, S., Horswill, A.R., et al. (2013). Bacteria activate sensory neurons that modulate pain and inflammation. Nature *501*, 52–57. https://doi.org/10.1038/nature12479.
2. Shah, A.S., Ben-Shahar, Y., Moninger, T.O., Kline, J.N., and Welsh, M.J. (2009). Motile cilia of human airway epithelia are chemosensory. Science *325*, 1131–1134. https://doi.org/10.1126/science.1173869.
3. Agduhr, E. (1922). Über ein zentrales Sinnesorgan (?) bei den Vertebraten. Z. Anat. Entwicklungsgesch. *66*, 223–360. https://doi.org/10.1007/BF02593586.
4. Kolmer, W. (1921). Das 'Sagitallorgan' der Wirbeltiere. Z. Anat. Entwickl. Gesch. *60*, 652–717.
5. Böhm, U.L., Prendergast, A., Djenoune, L., Nunes Figueiredo, S., Gomez, J., Stokes, C., Kaiser, S., Suster, M., Kawakami, K., Charpentier, M., et al. (2016). CSF-contacting neurons regulate locomotion by relaying mechanical stimuli to spinal circuits. Nat. Commun. *7*, 10866. https://doi.org/10.1038/ncomms10866.
6. Jalalvand, E., Robertson, B., Wallén, P., and Grillner, S. (2016). Ciliated neurons lining the central canal sense both fluid movement and pH through ASIC3. Nat. Commun. *7*, 10002. https://doi.org/10.1038/ncomms10002.
7. Orts-Del'Immagine, A., Cantaut-Belarif, Y., Thouvenin, O., Roussel, J., Baskaran, A., Langui, D., Koëth, F., Bivas, P., Lejeune, F.X., Bardet, P.L., and Wyart, C. (2020). Sensory neurons contacting the cerebrospinal fluid require the reissner fiber to detect spinal curvature in vivo. Curr. Biol. *30*, 827–839.e4.
8. Sternberg, J.R., Prendergast, A.E., Brosse, L., Cantaut-Belarif, Y., Thouvenin, O., Orts-Del'Immagine, A., Castillo, L., Djenoune, L., Kurisu, S., McDearmid, J.R., et al. (2018). Pkd2l1 is required for mechanoception in cerebrospinal fluid-contacting neurons and maintenance of spine curvature. Nat. Commun. *9*, 3804. https://doi.org/10.1038/s41467-018-06225-x.
9. Fidelin, K., Djenoune, L., Stokes, C., Prendergast, A., Gomez, J., Baradel, A., Del Bene, F., and Wyart, C. (2015). State-dependent modulation of locomotion by GABAergic spinal sensory neurons. Curr. Biol. *25*, 3035–3047. https://doi.org/10.1016/j.cub.2015.09.070.
10. Hubbard, J.M., Böhm, U.L., Prendergast, A., Tseng, P.B., Newman, M., Stokes, C., and Wyart, C. (2016). Intraspinal sensory neurons provide powerful inhibition to motor circuits ensuring postural control during locomotion. Curr. Biol. *26*, 2841–2853. https://doi.org/10.1016/j.cub.2016.08.026.
11. Wu, M.Y., Carbo-Tano, M., Mirat, O., Lejeune, F.X., Roussel, J., Quan, F.B., Fidelin, K., and Wyart, C. (2021). Spinal sensory neurons project onto the hindbrain to stabilize posture and enhance locomotor speed. Curr. Biol. *31*, 3315–3329.e5. https://doi.org/10.1016/j.cub.2021.05.042.
12. Cantaut-Belarif, Y., Orts Del'Immagine, A., Penru, M., Pézeron, G., Wyart, C., and Bardet, P.L. (2020). Adrenergic activation modulates the signal from the Reissner fiber to cerebrospinal fluid-contacting neurons during development. eLife *9*, e59469. https://doi.org/10.7554/eLife.59469.
13. Cantaut-Belarif, Y., Sternberg, J.R., Thouvenin, O., Wyart, C., and Bardet, P.L. (2018). The reissner fiber in the cerebrospinal fluid controls morphogenesis of the body axis. Curr. Biol. *28*, 2479–2486.e4. https://doi.org/10.1016/j.cub.2018.05.079.
14. Quan, F.B., Dubessy, C., Galant, S., Kenigfest, N.B., Djenoune, L., Leprince, J., Wyart, C., Lihrmann, I., and Tostivint, H. (2015). Comparative distribution and in vitro activities of the urotensin II-related peptides URP1 and URP2 in zebrafish: evidence for their colocalization in spinal cerebrospinal fluid-contacting neurons. PLoS One *10*, e0119290. https://doi.org/10.1371/journal.pone.0119290.
15. Zhang, X., Jia, S., Chen, Z., Chong, Y.L., Xie, H., Feng, D., Wu, X., Song, D.Z., Roy, S., and Zhao, C. (2018). Cilia-driven cerebrospinal fluid flow directs expression of urotensin neuropeptides to straighten the vertebrate body axis. Nat. Genet. *50*, 1666–1673. https://doi.org/10.1038/s41588-018-0260-3.

16. Lu, H., Shagirova, A., Goggi, J.L., Yeo, H.L., and Roy, S. (2020). Reissner fibre-induced urotensin signalling from cerebrospinal fluid-contacting neurons prevents scoliosis of the vertebrate spine. Biol. Open *9*, bio052027. https://doi.org/10.1242/bio.052027.

17. Alejevski, F., Leemans, M., Gaillard, A.L., Leistenschneider, D., de Flori, C., Bougerol, M., Le Mével, S., Herrel, A., Fini, J.B., Pézeron, G., et al. (2021). Conserved role of the urotensin II receptor 4 signalling pathway to control body straightness in a tetrapod. Open Biol. *11*, 210065. https://doi.org/10.1098/rsob.210065.

18. Bearce, E.A., Irons, Z.H., O'Hara-Smith, J.R., Kuhns, C.J., Fisher, S.I., Crow, W.E., and Grimes, D.T. (2022). Urotensin II-related peptides, Urp1 and Urp2, control zebrafish spine morphology. eLife *11*, e83883. https://doi.org/10.7554/eLife.83883.

19. Gaillard, A.-L., Mohamad, T., Quan, F.B., de Cian, A., Mosiman, C., Tostivint, H., and Pézeron, G. (2022). Urp1 and Urp2 act redundantly to maintain spine shape in zebrafish larvae. https://doi.org/10.1101/2022.08.09.503396.

20. Djenoune, L., Khabou, H., Joubert, F., Quan, F.B., Nunes Figueiredo, S., Bodineau, L., Del Bene, F., Burcklé, C., Tostivint, H., and Wyart, C. (2014). Investigation of spinal cerebrospinal fluid-contacting neurons expressing PKD2L1: evidence for a conserved system from fish to primates. Front. Neuroanat. *8*, 26. https://doi.org/10.3389/fnana.2014.00026.

21. Huang, A.L., Chen, X., Hoon, M.A., Chandrashekar, J., Guo, W., Tränkner, D., Ryba, N.J., and Zuker, C.S. (2006). The cells and logic for mammalian sour taste detection. Nature *442*, 934–938. https://doi.org/10.1038/nature05084.

22. Orts-Del'immagine, A., Wanaverbecq, N., Tardivel, C., Tillement, V., Dallaporta, M., and Trouslard, J. (2012). Properties of subependymal cerebrospinal fluid contacting neurones in the dorsal vagal complex of the mouse brainstem. J. Physiol. *590*, 3719–3741. https://doi.org/10.1113/jphysiol.2012.227959.

23. Hull, M., Parnes, M., and Jankovic, J. (2021). Botulinum neurotoxin injections in childhood opisthotonus. Toxins (Basel) *13*, 137. https://doi.org/10.3390/toxins13020137.

24. Jim, K.K., Engelen-Lee, J., van der Sar, A.M., Bitter, W., Brouwer, M.C., van der Ende, A., Veening, J.W., van de Beek, D., and Vandenbroucke-Grauls, C.M. (2016). Infection of zebrafish embryos with live fluorescent Streptococcus pneumoniae as a real-time pneumococcal meningitis model. J. Neuroinflammation *13*, 188. https://doi.org/10.1186/s12974-016-0655-y.

25. Zunt, J.R., Kassebaum, N.J., Blake, N., Glennie, L., Wright, C., Nichols, E., Abd-Allah, F., Abdela, J., Abdelalim, A., Adamu, A.A., et al. (2018). Global, regional, and national burden of meningitis, 1990–2016: a systematic analysis for the Global Burden of Disease Study 2016. Lancet Neurol. *17*, 1061–1082. https://doi.org/10.1016/S1474-4422(18)30387-9.

26. van de Beek, D., Brouwer, M., Hasbun, R., Koedel, U., Whitney, C.G., and Wijdicks, E. (2016). Community-acquired bacterial meningitis. Nat. Rev. Dis. Primers *2*, 16074. https://doi.org/10.1038/nrdp.2016.74.

27. van de Beek, D., Brouwer, M.C., Koedel, U., and Wall, E.C. (2021). Community-acquired bacterial meningitis. Lancet *398*, 1171–1183. https://doi.org/10.1016/S0140-6736(21)00883-7.

28. van de Beek, D., de Gans, J., Tunkel, A.R., and Wijdicks, E.F. (2006). Community-acquired bacterial meningitis in adults. N. Engl. J. Med. *354*, 44–53. https://doi.org/10.1056/NEJMra052116.

29. van de Beek, D., de Gans, J., Spanjaard, L., Weisfelt, M., Reitsma, J.B., and Vermeulen, M. (2004). Clinical features and prognostic factors in adults with bacterial meningitis. N. Engl. J. Med. *351*, 1849–1859. https://doi.org/10.1056/NEJMoa040845.

30. Zoons, E., Weisfelt, M., de Gans, J., Spanjaard, L., Koelman, J.H., Reitsma, J.B., and van de Beek, D. (2008). Seizures in adults with bacterial meningitis. Neurology *70*, 2109–2115. https://doi.org/10.1212/01.wnl.0000288178.91614.5d.

31. Budick, S.A., and O'Malley, D.M. (2000). Locomotor repertoire of the larval zebrafish: swimming, turning and prey capture. J. Exp. Biol. *203*, 2565–2579. https://doi.org/10.1242/jeb.203.17.2565.

32. Omdal, R. (2020). The biological basis of chronic fatigue: neuroinflammation and innate immunity. Curr. Opin. Neurol. *33*, 391–396. https://doi.org/10.1097/WCO.0000000000000817.

33. Gawel, K., Langlois, M., Martins, T., van der Ent, W., Tiraboschi, E., Jacmin, M., Crawford, A.D., and Esguerra, C.V. (2020). Seizing the moment: zebrafish epilepsy models. Neurosci. Biobehav. Rev. *116*, 1–20. https://doi.org/10.1016/j.neubiorev.2020.06.010.

34. Kadioglu, A., Weiser, J.N., Paton, J.C., and Andrew, P.W. (2008). The role of Streptococcus pneumoniae virulence factors in host respiratory colonization and disease. Nat. Rev. Microbiol. *6*, 288–301. https://doi.org/10.1038/nrmicro1871.

35. Filipiak, W., Sponring, A., Baur, M.M., Ager, C., Filipiak, A., Wiesenhofer, H., Nagl, M., Troppmair, J., and Amann, A. (2012). Characterization of volatile metabolites taken up by or released from Streptococcus pneumoniae and Haemophilus influenzae by using GC-MS. Microbiology (Reading) *158*, 3044–3053. https://doi.org/10.1099/mic.0.062687-0.

36. Freund, J.R., Mansfield, C.J., Doghramji, L.J., Adappa, N.D., Palmer, J.N., Kennedy, D.W., Reed, D.R., Jiang, P., and Lee, R.J. (2018). Activation of airway epithelial bitter taste receptors by Pseudomonas aeruginosa quinolones modulates calcium, cyclic-AMP, and nitric oxide signaling. J. Biol. Chem. *293*, 9824–9840. https://doi.org/10.1074/jbc.RA117.001005.

37. Lee, R.J., Chen, B., Redding, K.M., Margolskee, R.F., and Cohen, N.A. (2014). Mouse nasal epithelial innate immune responses to Pseudomonas aeruginosa quorum-sensing molecules require taste signaling components. Innate Immun. *20*, 606–617. https://doi.org/10.1177/1753425913503386.

38. Saunders, C.J., Christensen, M., Finger, T.E., and Tizzano, M. (2014). Cholinergic neurotransmission links solitary chemosensory cells to nasal inflammation. Proc. Natl. Acad. Sci. USA *111*, 6075–6080. https://doi.org/10.1073/pnas.1402251111.

39. Tizzano, M., Gulbransen, B.D., Vandenbeuch, A., Clapp, T.R., Herman, J.P., Sibhatu, H.M., Churchill, M.E., Silver, W.L., Kinnamon, S.C., and Finger, T.E. (2010). Nasal chemosensory cells use bitter taste signaling to detect irritants and bacterial signals. Proc. Natl. Acad. Sci. USA *107*, 3210–3215. https://doi.org/10.1073/pnas.0911934107.

40. Verbeurgt, C., Veithen, A., Carlot, S., Tarabichi, M., Dumont, J.E., Hassid, S., and Chatelain, P. (2017). The human bitter taste receptor T2R38 is broadly tuned for bacterial compounds. PLoS One *12*, e0181302. https://doi.org/10.1371/journal.pone.0181302.

41. Bos, L.D., Sterk, P.J., and Schultz, M.J. (2013). Volatile metabolites of pathogens: a systematic review. PLoS Pathog. *9*, e1003311. https://doi.org/10.1371/journal.ppat.1003311.

42. England, S.J., Campbell, P.C., Banerjee, S., Swanson, A.J., and Lewis, K.E. (2017). Identification and expression analysis of the complete family of zebrafish pkd genes. Front. Cell Dev. Biol. *5*, 5. https://doi.org/10.3389/fcell.2017.00005.

43. Petracca, Y.L., Sartoretti, M.M., Di Bella, D.J., Marin-Burgin, A., Carcagno, A.L., Schinder, A.F., and Lanuza, G.M. (2016). The late and dual origin of cerebrospinal fluid-contacting neurons in the mouse spinal cord. Development *143*, 880–891. https://doi.org/10.1242/dev.129254.

44. Andrzejczuk, L.A., Banerjee, S., England, S.J., Voufo, C., Kamara, K., and Lewis, K.E. (2018). Tal1, Gata2a, and Gata3 have distinct functions in the development of V2b and cerebrospinal fluid-contacting KA spinal neurons. Front. Neurosci. *12*, 170. https://doi.org/10.3389/fnins.2018.00170.

45. Shin, J., Poling, J., Park, H.C., and Appel, B. (2007). Notch signaling regulates neural precursor allocation and binary neuronal fate decisions in zebrafish. Development *134*, 1911–1920.

46. Yang, L., Rastegar, S., and Strähle, U. (2010). Regulatory interactions specifying Kolmer-Agduhr interneurons. Development *137*, 2713–2722. https://doi.org/10.1242/dev.048470.

47. Desban, L., Prendergast, A., Roussel, J., Rosello, M., Geny, D., Wyart, C., and Bardet, P.L. (2019). Regulation of the apical extension morphogenesis tunes the mechanosensory response of microvilliated neurons. PLoS Biol. *17*, e3000235. https://doi.org/10.1371/journal.pbio.3000235.

48. Christenson, J., Alford, S., Grillner, S., and Hökfelt, T. (1991). Co-localized GABA and somatostatin use different ionic mechanisms to hyperpolarize target neurons in the lamprey spinal cord. Neurosci. Lett. *134*, 93–97. https://doi.org/10.1016/0304-3940(91)90516-v.

49. Djenoune, L., Desban, L., Gomez, J., Sternberg, J.R., Prendergast, A., Langui, D., Quan, F.B., Marnas, H., Auer, T.O., Rio, J.P., et al. (2017). The dual developmental origin of spinal cerebrospinal fluid-contacting neurons gives rise to distinct functional subtypes. Sci. Rep. *7*, 719. https://doi.org/10.1038/s41598-017-00350-1.

50. Schotland, J.L., Shupliakov, O., Grillner, S., and Brodin, L. (1996). Synaptic and nonsynaptic monoaminergic neuron systems in the lamprey spinal cord. J. Comp. Neurol. *372*, 229–244. https://doi.org/10.1002/(SICI)1096-9861(19960819)372:2<229::AID-CNE6>3.0.CO;2-5.

51. Marquart, G.D., Tabor, K.M., Brown, M., Strykowski, J.L., Varshney, G.K., LaFave, M.C., Mueller, T., Burgess, S.M., Higashijima, S., and Burgess, H.A. (2015). A 3D searchable database of transgenic zebrafish Gal4 and Cre lines for functional neuroanatomy studies. Front. Neural Circuits *9*, 78. https://doi.org/10.3389/fncir.2015.00078.

52. Sternberg, J.R., Severi, K.E., Fidelin, K., Gomez, J., Ihara, H., Alcheikh, Y., Hubbard, J.M., Kawakami, K., Suster, M., and Wyart, C. (2016). Optimization of a neurotoxin to investigate the contribution of excitatory interneurons to speed modulation in vivo. Curr. Biol. *26*, 2319–2328. https://doi.org/10.1016/j.cub.2016.06.037.

53. Cropper, E.C., Jing, J., Vilim, F.S., and Weiss, K.R. (2018). Peptide co-transmitters as dynamic, intrinsic modulators of network activity. Front. Neural Circuits *12*, 78. https://doi.org/10.3389/fncir.2018.00078.

54. de Jong, E.K., Vinet, J., Stanulovic, V.S., Meijer, M., Wesseling, E., Sjollema, K., Boddeke, H.W., and Biber, K. (2008). Expression, transport, and axonal sorting of neuronal CCL21 in large dense-core vesicles. FASEB J. *22*, 4136–4145. https://doi.org/10.1096/fj.07-101907.

55. Moqbel, R., and Coughlin, J.J. (2006). Differential secretion of cytokines. Sci. STKE *2006*, pe26. https://doi.org/10.1126/stke.3382006pe26.

56. Murray, P.J., and Wynn, T.A. (2011). Protective and pathogenic functions of macrophage subsets. Nat. Rev. Immunol. *11*, 723–737. https://doi.org/10.1038/nri3073.

57. Brunger, A.T., Jin, R., and Breidenbach, M.A. (2008). Highly specific interactions between botulinum neurotoxins and synaptic vesicle proteins. Cell. Mol. Life Sci. *65*, 2296–2306. https://doi.org/10.1007/s00018-008-8088-0.

58. Allardyce, R.A., Langford, V.S., Hill, A.L., and Murdoch, D.R. (2006). Detection of volatile metabolites produced by bacterial growth in blood culture media by selected ion flow tube mass spectrometry (SIFT-MS). J. Microbiol. Methods *65*, 361–365. https://doi.org/10.1016/j.mimet.2005.09.003.

59. Lee, R.J., and Cohen, N.A. (2014). Sinonasal solitary chemosensory cells "taste" the upper respiratory environment to regulate innate immunity. Am. J. Rhinol. Allergy *28*, 366–373. https://doi.org/10.2500/ajra.2014.28.4077.

60. Yu, Y.X., Sun, X.H., Liu, Y., Pan, Y.J., and Zhao, Y. (2015). Odor fingerprinting of Listeria monocytogenes recognized by SPME-GC-MS and E-nose. Can. J. Microbiol. *61*, 367–372. https://doi.org/10.1139/cjm-2014-0652.

61. Passoni, G., Langevin, C., Palha, N., Mounce, B.C., Briolat, V., Affaticati, P., Job, E.D., Joly, J.S., Vignuzzi, M., Saleh, M.C., et al. (2017). Imaging of viral neuroinvasion in the zebrafish reveals that Sindbis and chikungunya viruses favour different entry routes. Dis. Model. Mech. *10*, 847–857. https://doi.org/10.1242/dmm.029231.

62. Shooshtarizadeh, P., Zhang, D., Chich, J.F., Gasnier, C., Schneider, F., Haïkel, Y., Aunis, D., and Metz-Boutigue, M.H. (2010). The antimicrobial peptides derived from chromogranin/secretogranin family, new actors of innate immunity. Regul. Pept. *165*, 102–110. https://doi.org/10.1016/j.regpep.2009.11.014.

63. Bertini, R., Howard, O.M., Dong, H.F., Oppenheim, J.J., Bizzarri, C., Sergi, R., Caselli, G., Pagliei, S., Romines, B., Wilshire, J.A., et al. (1999). Thioredoxin, a redox enzyme released in infection and inflammation, is a unique chemoattractant for neutrophils, monocytes, and T cells. J. Exp. Med. *189*, 1783–1789. https://doi.org/10.1084/jem.189.11.1783.

64. Chen, G., Zhao, J., Yin, Y., Wang, B., Liu, Q., Li, P., Zhao, L., and Zhou, H. (2014). C-type natriuretic peptide attenuates LPS-induced endothelial activation: involvement of p38, Akt, and NF-kappaB pathways. Amino Acids *46*, 2653–2663. https://doi.org/10.1007/s00726-014-1816-x.

65. Dalm, V.A., van Hagen, P.M., van Koetsveld, P.M., Achilefu, S., Houtsmuller, A.B., Pols, D.H., van der Lely, A.J., Lamberts, S.W., and Hofland, L.J. (2003). Expression of somatostatin, cortistatin, and somatostatin receptors in human monocytes, macrophages, and dendritic cells. Am. J. Physiol. Endocrinol. Metab. *285*, E344–E353. https://doi.org/10.1152/ajpendo.00048.2003.

66. Krantic, S. (2000). Peptides as regulators of the immune system: emphasis on somatostatin. Peptides *21*, 1941–1964.

67. Lee, R.J., Kofonow, J.M., Rosen, P.L., Siebert, A.P., Chen, B., Doghramji, L., Xiong, G., Adappa, N.D., Palmer, J.N., Kennedy, D.W., et al. (2014). Bitter and sweet taste receptors regulate human upper respiratory innate immunity. J. Clin. Invest. *124*, 1393–1405. https://doi.org/10.1172/JCI72094.

68. Ly, N.P., Komatsuzaki, K., Fraser, I.P., Tseng, A.A., Prodhan, P., Moore, K.J., and Kinane, T.B. (2005). Netrin-1 inhibits leukocyte migration in vitro and in vivo. Proc. Natl. Acad. Sci. USA *102*, 14729–14734. https://doi.org/10.1073/pnas.0506233102.

69. Pei, X., Sun, Q., Zhang, Y., Wang, P., Peng, X., Guo, C., Xu, E., Zheng, Y., Mo, X., Ma, J., et al. (2014). PC3-secreted microprotein is a novel chemoattractant protein and functions as a high-affinity ligand for CC chemokine receptor 2. J. Immunol. *192*, 1878–1886. https://doi.org/10.4049/jimmunol.1300758.

70. Tomasiuk, R., Lipowski, D., Szlufik, S., Peplinska, K., and Mikaszewska-Sokolewicz, M. (2016). Higher level of NT-proCNP in cerebrospinal fluid of patients with meningitis. Neurosci. Lett. *614*, 29–32. https://doi.org/10.1016/j.neulet.2015.12.053.

71. Jakutis, G., and Stainier, D.Y.R. (2021). Genotype-phenotype relationships in the context of transcriptional adaptation and genetic robustness. Annu. Rev. Genet. *55*, 71–91. https://doi.org/10.1146/annurev-genet-071719-020342.

72. Kashem, S.W., Riedl, M.S., Yao, C., Honda, C.N., Vulchanova, L., and Kaplan, D.H. (2015). Nociceptive sensory fibers drive interleukin-23 production from CD301b+ dermal dendritic cells and drive protective cutaneous immunity. Immunity *43*, 515–526. https://doi.org/10.1016/j.immuni.2015.08.016.

73. Talbot, S., Abdulnour, R.E., Burkett, P.R., Lee, S., Cronin, S.J., Pascal, M.A., Laedermann, C., Foster, S.L., Tran, J.V., Lai, N., et al. (2015). Silencing nociceptor neurons reduces allergic airway inflammation. Neuron *87*, 341–354. https://doi.org/10.1016/j.neuron.2015.06.007.

74. Foster, S.L., Seehus, C.R., Woolf, C.J., and Talbot, S. (2017). Sense and immunity: context-dependent neuro-immune interplay. Front. Immunol. *8*, 1463. https://doi.org/10.3389/fimmu.2017.01463.

75. Weinmaier, T., Riesing, M., Rattei, T., Bille, J., Arguedas-Villa, C., Stephan, R., and Tasara, T. (2013). Complete genome sequence of Listeria monocytogenes LL195, a serotype 4b strain from the 1983–1987 Listeriosis epidemic in Switzerland. Genome Announc. *1*. 16–12. https://doi.org/10.1128/genomeA.00152-12.

76. Hernandez, R., Sinodis, C., and Brown, D.T. (2010). Sindbis virus: propagation, quantification, and storage. Curr. Protoc. Microbiol. *Chapter 15*, Unit15B1. https://doi.org/10.1002/9780471729259.mc15b01s16.

77. Avery, O.T., Macleod, C.M., and McCarty, M. (1944). Studies on the chemical nature of the substance inducing transformation of pneumococcal types: induction of transformation by a desoxyribonucleic acid fraction isolated from pneumococcus type Iii. J. Exp. Med. *79*, 137–158. https://doi.org/10.1084/jem.79.2.137.

78. Slager, J., Aprianto, R., and Veening, J.W. (2018). Deep genome annotation of the opportunistic human pathogen Streptococcus pneumoniae D39. Nucleic Acids Res. *46*, 9971–9989. https://doi.org/10.1093/nar/gky725.

79. Kjos, M., Aprianto, R., Fernandes, V.E., Andrew, P.W., van Strijp, J.A., Nijland, R., and Veening, J.W. (2015). Bright fluorescent Streptococcus pneumoniae for live-cell imaging of host-pathogen interactions. J. Bacteriol. *197*, 807–818. https://doi.org/10.1128/JB.02221-14.

80. Beilharz, K., van Raaphorst, R., Kjos, M., and Veening, J.W. (2015). Red fluorescent proteins for gene expression and protein localization studies in Streptococcus pneumoniae and efficient transformation with DNA assembled via the Gibson assembly method. Appl. Environ. Microbiol. *81*, 7244–7252. https://doi.org/10.1128/AEM.02033-15.

81. Martin, B., García, P., Castanié, M.P., and Claverys, J.P. (1995). The recA gene of Streptococcus pneumoniae is part of a competence-induced operon and controls lysogenic induction. Mol. Microbiol. *15*, 367–379.

82. Scheer, N., Groth, A., Hans, S., and Campos-Ortega, J.A. (2001). An instructive function for Notch in promoting gliogenesis in the zebrafish retina. Development *128*, 1099–1107. https://doi.org/10.1242/dev.128.7.1099.

83. Renshaw, S.A., Loynes, C.A., Trushell, D.M., Elworthy, S., Ingham, P.W., and Whyte, M.K. (2006). A transgenic zebrafish model of neutrophilic inflammation. Blood *108*, 3976–3978. https://doi.org/10.1182/blood-2006-05-024075.

84. Schneider, C.A., Rasband, W.S., and Eliceiri, K.W. (2012). NIH Image to ImageJ: 25 years of image analysis. Nat. Methods *9*, 671–675. https://doi.org/10.1038/nmeth.2089.

85. Lawrence, C. (2011). Advances in zebrafish husbandry and management. Methods Cell Biol. *104*, 429–451. https://doi.org/10.1016/B978-0-12-374814-0.00023-9.

86. Lawrence, C. (2016). New frontiers for zebrafish management. Methods Cell Biol. *135*, 483–508. https://doi.org/10.1016/bs.mcb.2016.04.015.

87. Avery, O.T., Macleod, C.M., and McCarty, M. (1979). Studies on the chemical nature of the substance inducing transformation of pneumococcal types. Inductions of transformation by a desoxyribonucleic acid fraction isolated from pneumococcus type III. J. Exp. Med. *149*, 297–326. https://doi.org/10.1084/jem.149.2.297.

88. Manoli, M., and Driever, W. (2012). Fluorescence-activated cell sorting (FACS) of fluorescently tagged cells from zebrafish larvae for RNA isolation. Cold Spring Harb. Protoc. *2012*. pdb.prot069633. https://doi.org/10.1101/pdb.prot069633.

89. Morris, C.A., Benson, E., and White-Cooper, H. (2009). Determination of gene expression patterns using in situ hybridization to Drosophila testes. Nat. Protoc. *4*, 1807–1819. https://doi.org/10.1038/nprot.2009.192.

90. Thisse, C., and Thisse, B. (2008). High-resolution in situ hybridization to whole-mount zebrafish embryos. Nat. Protoc. *3*, 59–69. https://doi.org/10.1038/nprot.2007.514.

91. Vize, P.D., McCoy, K.E., and Zhou, X. (2009). Multichannel wholemount fluorescent and fluorescent/chromogenic in situ hybridization in Xenopus embryos. Nat. Protoc. *4*, 975–983. https://doi.org/10.1038/nprot.2009.69.

92. Bernardos, R.L., and Raymond, P.A. (2006). GFAP transgenic zebrafish. Gene Expr. Patterns *6*, 1007–1013. https://doi.org/10.1016/j.modgep.2006.04.006.

93. Johnson, K., Barragan, J., Bashiruddin, S., Smith, C.J., Tyrrell, C., Parsons, M.J., Doris, R., Kucenas, S., Downes, G.B., Velez, C.M., et al. (2016). Gfap-positive radial glial cells are an essential progenitor population for later-born neurons and glia in the zebrafish spinal cord. Glia *64*, 1170–1189. https://doi.org/10.1002/glia.22990.

94. Fisher, S., Grice, E.A., Vinton, R.M., Bessling, S.L., Urasaki, A., Kawakami, K., and McCallion, A.S. (2006). Evaluating the biological relevance of putative enhancers using Tol2 transposon-mediated transgenesis in zebrafish. Nat. Protoc. *1*, 1297–1305. https://doi.org/10.1038/nprot.2006.230.

95. Kwan, K.M., Fujimoto, E., Grabher, C., Mangum, B.D., Hardy, M.E., Campbell, D.S., Parant, J.M., Yost, H.J., Kanki, J.P., and Chien, C.B. (2007). The Tol2kit: a multisite gateway-based construction kit for Tol2 transposon transgenesis constructs. Dev. Dyn. *236*, 3088–3099. https://doi.org/10.1002/dvdy.21343.

96. Concordet, J.P., and Haeussler, M. (2018). CRISPOR: intuitive guide selection for CRISPR/Cas9 genome editing experiments and screens. Nucleic Acids Res. *46*, W242–W245. https://doi.org/10.1093/nar/gky354.

97. Auer, T.O., Xiao, T., Bercier, V., Gebhardt, C., Duroure, K., Concordet, J.P., Wyart, C., Suster, M., Kawakami, K., Wittbrodt, J., et al. (2015). Deletion of a kinesin I motor unmasks a mechanism of homeostatic branching control by neurotrophin-3. eLife *4*, 418. https://doi.org/10.7554/eLife.05061.

98. Boucontet, L., Passoni, G., Thiry, V., Maggi, L., Herbomel, P., Levraud, J.P., and Colucci-Guyon, E. (2018). A model of superinfection of virus-infected zebrafish larvae: increased susceptibility to bacteria associated with neutrophil death. Front. Immunol. *9*, 1084. https://doi.org/10.3389/fimmu.2018.01084.

99. Mirat, O., Sternberg, J.R., Severi, K.E., and Wyart, C. (2013). ZebraZoom: an automated program for high-throughput behavioral analysis and categorization. Front. Neural Circuits *7*, 107. https://doi.org/10.3389/fncir.2013.00107.

STAR★METHODS

KEY RESOURCES TABLE

REAGENT or RESOURCE	SOURCE	IDENTIFIER
Bacterial and virus strains		
Escherichia coli DH5α	ATCC	N/A
Listeria monocytogenes LL195	Weinmaier et al.[75]	N/A
Sindbis virus	Hernandez et al.[76]	N/A
Streptococcus pneumoniae D39V: serotype 2	Avery et al.[77] and Slager et al.[78]	N/A
Streptococcus pneumoniae D39V *hlpA*-GFP cam^r	Kjos et al.[79]	N/A
Streptococcus pneumoniae D39V *hlpA_hlpA*-mCherry cam^r	Beilharz et al.[80]	N/A
Chemicals, peptides, and recombinant proteins		
2-butanone	Sigma-Aldrich	Cat#W217012
2-methylpropanal	Sigma-Aldrich	Cat#W222003
2-pentanone	Sigma-Aldrich	Cat#W284220
α-bungarotoxin	Tocris Biosciences	Cat#2133
μ-Slide 8 Well	ibidi	Cat#80826
Acetone	Sigma-Aldrich	Cat#534064
B27 Supplement	Thermo Fisher Scientific	Cat#17504044
Bacto Brain Heart Infusion	Becton, Dickinson and Company	Cat#237500
C+Y medium	Martin et al.[81]	N/A
$CaCl_2$	Sigma-Aldrich	Cat#C3306
$CaCl_2$	Sigma-Aldrich	Cat#223506
Columbia agar, 5% v/v defibrinated sheep blood	bioMérieux	Cat#43049
Columbia Agar Base	Thermo Fisher Scientific	Cat# R452954
FBS	Thermo Fisher Scientific	Cat#10270106
Defibrinated Sheep Blood	bioTRADING	Cat#BTSG100
Dextran, Alexa Fluor 647; 10,000 MW, Anionic, Fixable	Invitrogen	Cat#D22914
Dimethyl disulfide (DMDS)	Sigma-Aldrich	Cat#W353604
DMEM	Thermo Fisher Scientific	Cat#10938025
DMSO	Sigma-Aldrich	Cat#D8418
Ethyl 3-aminobenzoate methanesulfonate	Sigma-Aldrich	Cat#A5040
Ethylenediaminetetraacetic acid disodium salt dihydrate (EDTA)	Sigma-Aldrich	Cat#E5134
FACSMax Buffer	AMC Biotechnology	Cat#T200100
Gibco Human GDNF Recombinant Protein	Fisher Scientific	Cat#10679963
Glass beads 1.0mm	Sigma-Aldrich	Cat#Z250473
D-(+)-Glucose	Sigma-Aldrich	Cat#G8769
D-(+)-Glucose	Sigma-Aldrich	Cat#G8270
HBSS	Fisher Scientific	Cat#14170088
HEPES	Sigma-Aldrich	Cat#H3375
KCl	Sigma-Aldrich	Cat#P9333
L-cysteine	Sigma-Aldrich	Cat#30089
L-glutamine	Thermo Fisher Scientific	Cat#25030024
Metronidazole	Sigma-Aldrich	Cat#M3761
$MgCl_2$	Sigma-Aldrich	Cat#M2670
N2 Supplement	Thermo Fisher Scientific	Cat#17502048
Na2HPO4	Sigma-Aldrich	Cat#5136
NaCl	Sigma-Aldrich	Cat#S7653
NaH2PO4	Sigma-Aldrich	Cat#4269

(*Continued on next page*)

Continued

REAGENT or RESOURCE	SOURCE	IDENTIFIER
NaOH	Sigma-Aldrich	Cat#71687
Neurobasal Medium	Thermo Fisher Scientific	Cat#10888022
NGF	Merck Millipore	Cat#01-125
Papain	Serlabo Technologies	Cat#WOLK03176-1
Paraformaldehyde	Sigma-Aldrich	Cat#158127
Penicillin/Streptomycin	Thermo Fisher Scientific	Cat#15140122
Phenol red solution	Sigma-Aldrich	Cat#P0290
Recombinant serotype 4 pneumolysin	MyBioSource	Cat#MBS1141054
Sea salts	Sigma-Aldrich	Cat#S9883
Sheep blood defibrinated	bioTRADING	Cat#BTSG10
Sodium pyruvate	Thermo Fisher Scientific	Cat#11360039
Streptococcus selective supplement (COBA)	Oxoid	Cat#SR0126
Sucrose	Sigma-Aldrich	Cat#S7903
Tricaine	Sigma-Aldrich	Cat#A5040
Critical commercial assays		
Clontech SMART-Seq v4 Kit	Clontech	Cat#634888
Gateway LR Clonase	Thermo Fisher Scientific	Cat#11791020
Illumina NextSeq 500	Illumina	Cat#SY-415-1001
Luminaris HiGreen qPCR Master Mix	Thermo Fisher Scientific	Cat#K0991
Nextera DNA Library Preparation Kit	Illumina	Cat#FC-131-1024
RNAeasy Micro Kit	Qiagen	Cat#74004
RNAeasy Mini Kit	Qiagen	Cat#74104
SMART-Seq v4 PLUS kit	Takara Bio	Cat#R400752
SuperScript IV First-Strand Synthesis System	Thermo Fisher Scientific	Cat#18091050
SuperScript IV VILO	Invitrogen	Cat#11756050
TOPO-TA for subcloning	Thermo Fisher Scientific	Cat#451641
Experimental models: Cell lines		
BHK-21 cells	ATCC	Cat#CCL-10; RRID:CVCL_1915
Experimental models: Organisms/strains		
Zebrafish: *AB* wild-type	N/A	ZFIN: ZDB-GENO-960809-7
Zebrafish: *pkd2l1*^{icm02}	Böhm et al.[5]	ZFIN: ZDB-ALT-160119-6
Zebrafish: *scg2a* mutant allele	This paper	*scg2a*^{icm71}
Zebrafish: *nppc* mutant allele	This paper	*nppc*^{icm36}
Zebrafish: *esm1* mutant allele	This paper	*esm1*^{icm34}
Zebrafish: *tas2r3a* mutant allele	This paper	*tas2r3a*^{icm64}
Zebrafish: *tas2r3b* mutant allele	This paper	*tas2r3b*^{icm65}
Zebrafish: *Tg(pkd2l1:GCaMP5G)*^{icm07}	Böhm et al.[5]	ZFIN: ZDB-ALT-160119-4
Zebrafish: *Tg(UAS:GCaMP5G)*^{icm08}	Fidelin et al.[9]	ZFIN: ZDB-ALT-150417-4
Zebrafish: *Tg(pkd2l1:Gal4)*^{icm10}	Fidelin et al.[9]	ZFIN: ZDB-ALT-150324-1
Zebrafish: *Tg(UAS:BoTxBLC-GFP)*^{icm21}	Sternberg et al.[52]	ZFIN: ZDB-ALT-160119-9
Zebrafish: *Tg(mnx1:Gal4)*^{icm23}	Böhm et al.[5]	ZFIN: ZDB-ALT-160120-1
Zebrafish: *Tg(GFAP:Gal4)*^{icm47}	This paper	ZFIN: ZDB-ALT-190115-1
Zebrafish: *Tg(UAS:epNTR-tagRFP-UTR.zb3)*^{y362}	Marquart et al.[51]	ZFIN: ZDB-ALT-160830-1
Zebrafish: *Tg(UAS:GFP)*^{kca33}	Scheer et al.[82]	ZFIN: ZDB-ALT-030716-2
Zebrafish: *Tg(UAS:tagRFP)*	Böhm et al.[5]	N/A
Zebrafish: *Tg(mpx:GFP)*^{i114}	Renshaw et al.[83]	ZFIN: ZDB-FISH-161202-8
Oligonucleotides		
scg2a F1 - TTTTTCTCTCTCATGTAAATCTGTCTG	This paper	N/A
scg2a R1 - GAGATGCCATTTTAAGCACTGAAC	This paper	N/A

(*Continued on next page*)

Continued

REAGENT or RESOURCE	SOURCE	IDENTIFIER
scg2a F2 - AAATTTATCCGGATTAGTGTAGACATG	This paper	N/A
scg2a R2 - ATAAGAAACGGGTTCAGTTCCACTAAG	This paper	N/A
nppc F1 - TGTTGATTTTAAGTCATAGGCTACATG	This paper	N/A
nppc R1 - TTAAAGCAGCTTTTCTTTTTAACACTG	This paper	N/A
nppc F2 - GAGAGGTTGTTAATGGAGTGGTAG	This paper	N/A
nppc R2 - TAGAGTGAATCCAGAGTCATTATGAAG	This paper	N/A
esm1 F1 - ATAATCATCCTCATCCTTGTAGAAGTC	This paper	N/A
esm1 R1 - CTTCATTCACTGTCACATCCAAGGAG	This paper	N/A
tas2r3 F1 - TAATGTTTTACTGTGGTCACTTATTGG	This paper	N/A
tas2r3 R1 - AAACACAACCTCGAATAGACATATATG	This paper	N/A
scg2a crRNA1 - GCTGGGAGGAGGGCGCAATT	This paper	N/A
scg2a crRNA2 - TCATCTCGATGCTGCGCAGC	This paper	N/A
nppc crRNA1 - CAGCAAATGCGAGATGATCA	This paper	N/A
nppc crRNA2 - ACACTCGGGCACGGGGCCCC	This paper	N/A
esm1 crRNA1 - GACTGAGGCGTGGGGTCCCG	This paper	N/A
esm1 crRNA2 - GCAGTGCTCACCCCGTCCCG	This paper	N/A
tas2r3 crRNA1 - ATGACTGAAATTCCTGCAGC	This paper	N/A
tas2r3 crRNA2 - TCCAGACCAAAAACGGCCAC	This paper	N/A
Software and algorithms		
Illustrator	Adobe	https://www.adobe.com/
ImageJ	Schneider et al.[84]	https://imagej.nih.gov/ij
MATLAB	Mathworks	N/A
Prism 7.0	GraphPad	https://www.graphpad.com/
Other		
Gemma Micro 500	Skretting	N/A

RESOURCE AVAILABILITY

Lead contact

Further information and requests for resources and reagents should be directed to and will be fulfilled by the lead contact, Claire Wyart (claire.wyart@icm-institute.org).

Materials availability

- Plasmids used in this study are available on request.
- Zebrafish lines generated in this study are available on request.
- This study did not generate new reagents.

Data and code availability

- All tabulated RNAseq results are provided as Data S1; the raw data are available from the lead contact upon request.
- all MATLAB code used for analysis can be obtained at https://github.com/wyartlab
- Any additional information required to reanalyze the data reported in this paper is available from the lead contact upon request.

EXPERIMENTAL MODEL AND SUBJECT DETAILS

Zebrafish handling and husbandry

Zebrafish adults were maintained on a 14h/10h light/dark cycle and fed using a combination of Gemma Micro 500 diet and cultured rotifers.[85,86] All embryos and larvae described in this study were obtained by natural mating procedures. Animals were used for experiments until no later than 6 days post fertilization. All experimental procedures comply with European animal welfare regulations.

Bacterial strains and growth conditions

Streptococcus pneumoniae D39 serotype 2 wild-type strain, the isogenic red fluorescent *S. pneumoniae* D39 HlpA-mCherry mutant strain, or green fluorescent *S. pneumoniae* D39 HlpA-GFP mutant strain, in which the fluorescent proteins are fused to the histone-like protein, was grown on Columbia agar supplemented with 5% (v/v) defibrinated sheep blood (Biomerieux; 43049) at 37°C in a humidified atmosphere with 5% CO_2.[78,80,87] The *Listeria monocytogenes* LL195 wild-type strain was grown on Columbia agar supplemented with 5% (v/v) defibrinated sheep blood at 37°C.[75] Before injection, *S. pneumoniae* or *L. monocytogenes* was grown to mid log phase in C+Y medium[81] or BHI medium respectively at 37°C. Bacteria were subsequently harvested by centrifugation (6000 rpm, 10 min for *S. pneumoniae*, 4000 RPM for 5 min for *L. monocytogenes*) and suspended in sterile 0.5% (w/v) phenol red solution in PBS (Sigma-Aldrich, P0290) to aid visualization of the injection process.[24] Note that at this concentration, the use of phenol red for injections did not affect bacterial growth during the pre-injection interval.

Primary cell culture of CSF-cNs

We adapted a two-step culture protocol previously published comprising an initial feeder layer of cells on which were plated a second layer of fluorescent positives CSF-cNs cells.[8] Briefly, all embryos were bleached prior to dissociation in 0.003% bleach in reverse osmosis water in order to avoid contaminations. To perform the initial feeder layer of cells, we dissociated 2 dpf AB WT embryos using papain at 20U/mL (Serlabo Technologies, WOLK03176-1) in HBSS 1X solution (Fisher Scientific, 14170088) complemented with 0.2 mg/mL cysteine (Sigma-Aldrich, 30089), 1.25 μM $CaCl_2$ (Sigma, C3306), 0.5 μM EDTA (Sigma-Aldrich, E5134), and 2 μM NaOH at 37° for 20 minutes. Dissociated cells were rinsed using HBSS 1X and plated overnight at a concentration of 1.10^6 cells/well in DMEM medium (ThermoFisher, 10938025) complemented with 2mM L-Glutamine (Thermo Fisher Scientific, 25030024), 50U/mL penicillin/streptomycin (Thermo Fisher Scientific, 15140122), 25ng/mL NGF (Merckmillipore, 01-125), 4ng/mL GDNF (Fisher Scientific, 10679963), 25mM glucose (Sigma-Aldrich, G8769-100ML), and 10% FBS (Thermo Fisher Scientific, 10270106). 24 hours after the initial feeder layer plating, we dissociated 3 dpf *Tg(pkd2l1:tagRFP, pkd2l1:GCaMP5G)* double transgenic embryos using the same 20u/mL papain complemented solution used for the initial layer. Dissociated cells were rinsed using HBSS 1X and plated overnight at a concentration of 5.10^5 cells/well in Neurobasal medium (Thermo Fisher Scientific, 10888022), complemented with 1X B27 supplement (Thermo Fisher Scientific, 17504044), 1X N2 supplement (Thermo Fisher Scientific, 17502048), 2 mM L-glutamine (Thermo Fisher Scientific, 25030024), 10 U/mL penicillin/streptomycin (Thermo Fisher Scientific, 15140122), decomplemented FBS (Thermo Fisher Scientific, 10270106), and 1 mM sodium pyruvate (Thermo Fisher Scientific, 11360039). Cells were used 48 hours after the plating of the second layer.

METHOD DETAILS

Confocal imaging

All widefield confocal imaging was either performed live or mounted in 1.5% agarose on a Nikon ECLIPSE Ti2 inverted microscope (Figure 1), a Nikon AIR confocal microscope system (Figure 2), a 3i VIVO spinning disk microscope (Figure 6), or fixed and mounted in 50% glycerol on a Zeiss LSM5 Pascal confocal microscope (Figure 4).

Bacterial load

We injected zebrafish larvae with *S. pneumoniae* D39 wild-type strain into the hindbrain ventricle (see Table S1 for a summary of all conditions used in imaging and survival experiments) and determined the bacterial load in whole infected zebrafish larvae homogenates at 24 hours post injection (hpi). At 24 hpi, infected zebrafish larvae were anesthetized in 0.02 % Tricaine (Sigma-Aldrich A5040), transferred to a 1.5 ml screwcap tube (1 larva per tube) filled with 1.0 mm glass beads (Sigma-Aldrich Z250473) to ~25% capacity of the tubes volume, placed in a microvial rack, and violently shaken (3 times 10 sec, 10 sec interval) in a bead beater (Biospec Products; Mini Beadbeater) to disrupt the cells and tissues. Subsequently, serial dilution plating of the homogenates was performed on Columbia Blood Agar (Thermo Fisher, R452954) plates supplemented with 5% defibrinated sheep blood (bioTRADING, BTSG10), 10 mg/ml colistin sulphate and 5 mg/ml oxolinic acid (COBA, Oxoid), to inhibit growth of commensal bacteria in zebrafish. The plates were incubated O/N at 37°C and quantified the next day. All experiments were performed in duplicate.

Simulations of *in vitro* CSF-cN stimulation

In order to estimate the concentration of molecules at the surface of the CSF-cN during and after the 1-second stimulus, we carried out numerical simulations applying finite-element method (Comsol Multiphysics, Transport of Diluted Species & Laminar Flow modules). We here describe the model in more details. The concentration of molecules c obeys the advection-diffusion law:

$$\frac{\partial c}{\partial t} + v \cdot \nabla c - D\Delta c = 0$$

where D is the diffusion coefficient of the molecule, ∇ is the differential operator and Δ is the Laplacian operator. Here v is the fluid velocity vector obeying the incompressible Navier-Stokes equations:

$$\rho \nabla \cdot (v) = 0$$

$$\rho\frac{\partial v}{\partial t} + \rho(v\cdot\nabla)v = -\nabla.\sigma + \mu\Delta v$$

where $\rho = 10^3$ kg/m is the water density and $\sigma = -pI + \mu\nabla u + \mu(\nabla u)^T$ is the total stress tensor, with $\mu = 10^{-3}$ Pa.s the water viscosity and I the identity matrix. Bold terms represent three dimensional vectors or tensors.

The flow is simulated in a cylindrical container of height 0.45 mm and diameter 2 mm. Note that the concentration distribution around the cell was found not to depend on the size of the container when the diameter exceeds 1.2 mm, which is smaller than the selected value. Inside this container, the initial concentration c_0 is set to 0. A flow of concentration c_{puff} passes through a spherical opening of diameter 3 μm, representing the stimulation pipette, with a flow rate of 3.6 nL/s during 1s, in the direction of the cell. The cell is represented by a portion of sphere of diameter 10 μm and of height above the floor plate 8 μm. The cell is located at a distance of 100 μm from the stimulation pipette.

Concerning the boundary conditions for the flow and the concentration, a no slip is imposed at the bottom wall and on the cell ($v = 0$), and a complete impermeability is imposed against the passage of molecules ($n\cdot(D\nabla c + cv) = 0$). The lateral walls as well as the upper wall of the cylindrical container are at imposed constant pressure p_0, and we impose the absence of concentration gradients $n\cdot\nabla c = 0$.

Numerically, the transition between the stimulus process (which lasts 1s) and the post-stimulus phase (t > 1s) is achieved via a smoothing function:

$$f(t) = \exp\left(-\left(\frac{t-1}{\tau}\right)^2\right), \text{with } \tau = 17 \text{ ms}$$

The number of tetrahedral mesh elements varies between 685000 and 850000 in the simulations presented in this manuscript. All the simulations converged, and doubling the number of mesh elements led to similar results.

Fluorescence activated cell sorting of CSF-cNs and validation

50 to 300 *Tg(pkd2l1:GAL4, UAS:GFP)* zebrafish larvae expressing green fluorescent protein (GFP) in cerebrospinal fluid-contacting neurons (CSF-cNs) were collected at 3 days post fertilization (dpf), anaesthetized in 0.02 % (w/v) buffered 3-aminobenzoic acid methyl ester (pH 7.0) (Tricaine; Sigma-Aldrich, A5040) and decapitated at the level of the hindbrain. The remaining trunk tissue was immediately de-yolked (in de-yolking buffer: 55 mM NaCl, 1.8 mM KCl, 1.25 mM $NaHCO_3$) and manually dissociated in FACSMax buffer (AMS Biotechnology, T200100) through a 30 μm sterile filter as described previously.[88] The resulting suspension was re-filtered and then sorted on a BD Biosciences FACS Jazz sorter to isolate CSF-cNs (between 3000-15000 cells/run, ~0.2% of total input). Cells were sorted directly into lysis buffer (Qiagen, 74004; Clontech, 634894) for both qRT-PCR validation and RNAseq library preparation; sorting runs were either entirely diverted to validation or library preparation as cell yield was insufficient to perform both analyses on the same sample. In each sorting run, we isolated separate populations of putative CSF-cNs and an assortment of other, GFP- cell types as a reference population (referred to as "green" and "dark" cells, respectively throughout this manuscript). To verify that a highly enriched population of CSF-cNs was being isolated prior to library preparation, several sorting runs were diverted to qRT-PCR analysis. These cells were converted to cDNA using the RNeasy Micro kit (Qiagen, 74004) followed by the VILO RT kit (Thermo Fisher, 11756500). qRT-PCR was performed comparing the relative expression of a panel of diagnostic transcripts including known CSF-cN-specific genes between "green" and "dark" cDNA pools using SYBR Green chemistry (Thermo Fisher, K0991). Previously known CSF-cN markers, such as *pkd2l1*[20,21] and *pkd1l2*,[42,43] were massively upregulated while markers of hindbrain cells (*raraa*, *rarab*) were not.

Library preparation and RNAseq (differential CSF-cN RNAseq)

Following validation by qPCR, five additional RNA pools were generated from both "dark" and "green" cells isolated by sorting on five different experimental days (since RNA yield was too low to split the pool for validation and sequencing). The SMART-Seq v4 Ultra Low Input kit (Qiagen, 74004) was used to generate double-stranded cDNA from each sorting replicate; these pools were fragmented and tagged for sequencing using the Nextera DNA Library Preparation Kit (Illumina). Finally, the prepared library was sequenced on an Illumina NextSeq 500 (SY-415-1001).

Fluorescent *in situ* hybridization and immunohistochemistry

cDNA was generated from 3 dpf AB larvae using the RNeasy Mini Kit (Qiagen, 74104) and SuperScript IV reverse transcriptase (Thermo Fisher, 18091050). DNA fragments from a subset of ~40 candidate genes derived from the RNAseq hitlist were amplified from this cDNA by PCR and cloned into TOPO vectors (Thermo Fisher, 451641). Antisense digoxigenin-incorporating probes were transcribed from these clones and hydrolyzed to ~300 bp as previously described.[89–91] To verify that these transcripts were enriched in CSF-cNs, we combined fluorescent *in situ* hybridization and immunohistochemistry for GFP in *Tg(pkd2l1:GCaMP5G)* or *Tg(mnx1:GCaMP5)* transgenic animals at 24 hours post fertilization (hpf) and adult stages as previously described.[20,49,90,91]

Generation of transgenic zebrafish lines

To generate a Tol2 vector driving GAL4 under the control of GFAP regulatory elements, we used Gateway recombination-based cloning (Thermo Fisher, 11791020) using p5E-GFAP, which contains 7.4 Kb of GFAP intron 1 and exon 1,[92,93] pME-GAL4, and

p3E-poly(A) into pDestpA2. The resulting vector was injected into *Tg(UAS:RFP; cryAA:Venus)* at 30 ng/μL with 35 ng/μL Tol2 transposase to generate germline transgenics as previously described.[94,95]

Generation of *tas2r3* mutants

Site-specific crRNAs were designed targeting the *tas2r3* coding sequence using the CRISPOR web tool[96] (IDT). These were then annealed to a common tracRNA component to form an RNA duplex stock (33 μM) which was then complexed with 10 μg/μL Alt-R-S.p. Cas9 Nuclease V3 (IDT) in Cas9 buffer (20 mM HEPES, 150 mM KCl, pH 7.5) at a 1:1 molar ratio according to the manufacturer's instructions. Zebrafish embryos were obtained at the 1-2 cell stage and 1 nL of the described mixture was injected into each embryo. Embryos were allowed to recover in E3 medium. ~10 embryos were collected at 1-3 days post fertilization (dpf) and their DNA was harvested by proteinase K digest and gRNAs were validated using an EaeI restriction cleavage site present in the crRNA binding region that would be disrupted by indel mutations caused by CRISPR/Cas9 modification. As noted in Figure S6, we would later find that *tas2r3* is present in our wild type background as at least two different paralogous alleles, which we were able to independently mutate and segregate in genotyping assays using paralog-specific PCR.

Generation of mutants in genes encoding CSF-cN neuropeptides

To generate *scg2a, nppc, esm1* null mutant line, we used the CRISPR/Cas9-mediated genome editing method. crRNA were designed by using online CRISPOR program (crispor.tefor.net/). crRNA and tracRNA were ordered from Integrated DNA Technology. The guiding RNA (key resources table) complex is prepared by duplex buffer, and mixed with Cas9 protein provided by Dr. Jean-Paul Concordet (MNHN, Paris, France). The mixed complex was injected into one-cell stage wild type eggs. The editing efficiency was tested after injection at 2 dpf by performing genotyping on 3 pools of 20 embryos. Genomic DNA was extracted in lysis buffer (10 mM Tris pH 8.2 mM EDTA, 0.2% Triton X-100, 200 μg/mL Proteinase K) at 55°C for 2 h followed by 10 min of deactivation at 99°C. Then the target region was amplified by performing PCR with specific primers (key resources table). The F0 generation which contains high efficiency mutations was raised to sexual maturity. The best transmitters were selected by screening the rate of mutation in F1 embryos. The mutations of F1 adult fish have been analyzed by sequencing the subcloned PCR product. The F1 fish that carried the best type of the mutation has been chosen and raised by crossing with AB wild type fish to generate the F2 fish. Analyzing enzymatic restriction digest in the targeted site was used to screen the homozygote, heterozygote, and wild type F2 fish.

scg2a encodes a precursor of 540 amino acids in a single exon. The beginning of this exon was targeted by two gRNAs. To generate the *scg2a*^{icm42} mutant allele, sequence analysis revealed that 10 nucleotides were deleted by the gRNA1/Cas9 complex, leading to a frameshift and a premature STOP codon leading to a truncated amino acid sequence deprived of the mature peptide precursor sequence. The Nppc precursor is encoded by 3 exons and the mature peptide sequence is contained in the second exon. To generate the *nppc*^{icm36} mutant allele, we targeted the beginning of the first exon in order to disrupt the signal peptide sequence. The gRNA/Cas9 complex we used mediated a 3 nucleotide deletion that led to a mutation on the start codon (from ATG to ATT), hindering the translation of first exon. The *esm1* gene is composed of 3 exons and encodes a 139 amino acids protein whose binding domain is encoded by exon1. The gRNA1/Cas9 complex we used induced an insertion of 13 nucleotides, which led to frame shift and premature STOP codon forming a truncated protein of 29 amino acids devoid of the binding domain in the *esm1*^{icm34} mutant allele.

Calcium imaging of zebrafish larvae after injections in the hindbrain ventricle

Transgenic zebrafish larvae expressing GCaMP in a cell-type specific manner—*Tg(pkd2l1:GCaMP5)* transgenic larvae for CSF-cNs and *Tg(GFAP:GAL4, UAS:GCaMP5G)* for ependymal radial glia—were anesthetized in tricaine and paralyzed with α-bungarotoxin (1mM, 1nL, Tocris Biosciences, 2133) i.m. or i.v. for imaging. Subsequently, the larvae were embedded in 1.5% low-melting point agarose dissolved in egg water (60 μg/mL sea salts, Sigma-Aldrich, S9883) in MilliQ) in an open uncoated 8-well chamber slide (ibidi, 80826) and kept at 28°C in a temperature-controlled chamber (Okolab). Larvae were imaged on a Nikon AIR confocal microscope system. FIJI/MATLAB was used for image analysis. Imaging involved several experimental conditions, unless otherwise noted, all solutions were injected into the hindbrain ventricle of 2 dpf larvae.

Pneumococcal meningitis

2000 colony forming units (CFU) of red fluorescent *S. pneumoniae* D39 HlpA-HlpA-mCherry or vehicle-injected with sterile 0.5% (w/v) phenol red solution in PBS were injected into the hindbrain ventricle after anesthesia of zebrafish larvae with tricaine followed by paralysis with α-bungarotoxin injection, before being embedded in low-melting point agarose as described previously.[24,80]

Heat-killed S. pneumoniae

Bacteria were prepared as above, except the culture was incubated for 20 minutes at 80° C prior to injection.

E. coli

A culture of DH5α *E. coli* (ATCC) was grown to OD_{600} 0.6. 1 nL of this culture was injected into the hindbrain ventricle as above.

Listerial meningitis

6000 CFU of *L. monocytogenes* LL195 or vehicle-injected with sterile 0.5% (w/v) phenol red solution in PBS were injected into the hindbrain ventricle after anesthesia of zebrafish larvae with tricaine followed by paralysis with α-bungarotoxin injection, before being embedded in low-melting point agarose.

Calcium imaging in primary cell culture

Calcium imaging on GCaMP5G-expressing neurons from the *Tg(pkd2l1:GCaMP5G)* transgenic line was performed on an epifluorescence microscope equipped with a Lumen Dynamics XT600 Xenon lamp and a GFP filter cube. Acquisition was performed at 5 Hz using an EM-CCD Camera from Hamamatsu. Puffs stimuli were delivered using a 1 s long TTL pulse from a Digidata acquisition system (Axon Instruments) and repeated 3 times with an inter trial interval of 64 seconds.

aCSF

Artificial CSF (aCSF) was composed of NaCl 140mM (Sigma-Aldrich, S7653), KCl 1mM (Sigma-Aldrich, P9333), $CaCl_2$ 2.5mM (Sigma-Aldrich, 223506), $MgCl_2$ 1mM (Sigma-Aldrich, M2670), HEPES 10mM (Sigma-Aldrich, H3375), D-(+)-Glucose 10mM (Sigma-Aldrich, G8270), diluted in MilliQ water; pH was adjusted at 7.4.

Pneumolysin

Recombinant serotype 4 pneumolysin purified from *E. coli* (MyBioSource, MBS1141054) was reconstituted in aCSF at a concentration of 0.1 mg/mL. In our *in vitro* experiments, the concentration of pneumolysin applied onto the cultured CSF-cNs was 50 μg/mL, which exceeds the threshold for 100% hemolytic activity more than threefold.

Mix of bitter compounds

Acetone (Sigma, 534064), 2-butanone (Sigma, W217012), 2-pentanone (Sigma, W284220), dimethyl disulfide (Sigma, W353604), 2-methylpropanal (Sigma, W222003) were diluted as a mix of bitter compounds in aCSF at a concentration of 100mM each. In our *in vitro* experiments, the concentration of each bitter compound applied onto the cultured CSF-cNs was 50 mM according to *in silico* simulations (Figure 3).

Dimethyl disulfide (DMDS) and 2-pentanone

DMDS (Sigma-Aldrich, W353604) and 2-pentanone (Sigma-Aldrich, W284220) were diluted in aCSF at 25, 50 and 100mM concentrations. In our *in vitro* experiments, the concentrations of DMDS and 2-pentanone applied onto the cultured CSF-cNs were 12.5, 25 and 50 mM according to *in silico* simulations (Figure 3).

Acetone, 2-butanone and 2-methylpropanal

Acetone (Sigma-Aldrich, 534064), 2-butanone (Sigma-Aldrich, W217012) and 2-methylpropanal (Sigma-Aldrich, W222003) were diluted in aCSF at 100 mM concentration. In our *in vitro* experiments, the concentration of acetone, 2-butanone and 2-methylpropanal applied onto the cultured CSF-cNs was 50 mM according to *in silico* simulations (Figures 3 and S2).

Supernatant after viral infection

Baby hamster kidney (BHK) cells were infected *in vitro* for 48 hours with Sindbis virus expressing the fluorescent protein mCherry. Uninfected cells were used as control group. After 48 hours, infected BHK cells showed red fluorescence and were detaching from their support, signs of infection of the cells by Sindbis virus – while control unifected cells did not show adhesion problem. Supernatants of control and infected cells were collected and inactivated by UV irradiation before pressure-applications.

S. pneumoniae *supernatant*

Cell-free culture supernatant produced by *S. pneumoniae* was obtained by growing *S. pneumoniae* D39 wild-type bacteria until the end of the mid-log growth phase in C+Y medium, supplemented with 0.8% yeast extract instead of 2.5% yeast extract to minimize autofluorescence of the medium while retaining optimal growth conditions for the bacteria. The culture was then centrifuged for 15 minutes at 5000 x *g*, and subsequently the supernatant was collected and filtered through a 0.22μM filter to remove residual bacterial cells before pressure-applications.

FACS sorting of infected larvae

Larvae were injected with 2000 CFU *S. pneumoniae* D39 wild-type strain as described above, collected at 24 hours post infection, and a single-cell suspension was generated using the same protocol as for prior rounds of FACS. Analysis and isolation were performed using a BD InFlux cell sorter controlled by BD FACS Sortware v1.2.0.142 software. Infected neurons were identified by eGFP reporter protein which was excited by a 488nm, 200mW laser and detected through a 530/40 bp filter. Cell auto-fluorescence was also excited by the 488nm laser and detected through a 692/40 bp filter. Live and intact cells were identified by DAPI staining and excited by a 405nm, 100mW laser. For gating and trigger thresholds, background particulate was identified by running cell suspension buffer alone and standard FSC vs SSC gating was applied to select whole, intact events of similar scatter properties. Live cells were then gated according to low DAPI signal events withing a distinct event cluster and, from there, 2 separate auto-fluorescent populations were sorted from the eGFP positive events. eGFP gating edges were set with no-color and eGFP FMO controls. Compensation was not applied to any parameters.

Library preparation and RNAseq (uninfected vs. infected CSF-cNs)

Three RNA pools were generated from both ''dark'' and ''green'' cells isolated in control and infected conditions by sorting. The SMART-Seq v4 Ultra Low Input kit (Clontech, 634888) was used to generate double-stranded cDNA from each sorting replicate; these pools were fragmented and tagged for sequencing using the Nextera XT DNA Library Preparation Kit (Illumina). Finally, the prepared library was sequenced on an Illumina NovaSeq 6000 SP (200 cycles, up to 800 million reads, Illumina).

RNAseq (uninfected vs. infected CSF-cNs) analysis using DESeq2

Differential expression (DE) analysis of uninfected vs. infected CSF-cNs RNAseq data was conducted in R version 3.6.1 (R Development Core Team, 2019) using the DESeq2 Bioconductor package (v1.26.0). From the raw count data, the DESEeq function performs

all the processing steps from the normalization of the counts with the calculation of size factors (accounting for differences in library sizes) and dispersion factors to the differential analysis itself. DE genes between infected and control cells were explored separately within each population of green and dark cells, and also for the difference of variation observed in the two populations (testing the "ratio of ratios": i.e. the Infected/Control ratio in the green cells divided by the Infected/Control ratio in the dark cells). Significant DE genes were determined by fitting Negative Binomial Generalized Linear Models (one model per gene), followed by a Wald test on the model coefficients for significance testing. To control for the false discovery rate (FDR), all p-values were adjusted using the Benjamini-Hochberg (BH) procedure, and all DE genes with a BH-adjusted p-value < 0.05 were considered statistically significant. Within each population of green and dark cells, the directional change of the DE gene expression level was indicated by the sign of the log fold: either positive when the average expression level in the infected cells was significantly higher than that in the control cells ("up in infected"); or negative when expression level was decreased in the infected cells ("down in infected").

Larval zebrafish survival assays

Survival (death here is defined as larvae that do not respond to tail touches nor have a beating heart) was assessed every 24 hours. Curves were generated with GraphPad Prism 7.0 and survival data were analyzed with the log rank (Mantel-Cox) test.

Survival experiments in CSF-cN compromised transgenic larvae

Zebrafish larvae were infected as described previously by injecting 2000 colony forming units (CFU) wild-type *S. pneumoniae* D39 into the hindbrain ventricle and kept in 6-well plates at 28°C with 20 larvae in each group per well.[24] The mortality rate was scored by monitoring live and dead embryos at 24 hours intervals post-injection; mortality was determined by heartbeat and response mechanical stimuli. All experiments were performed in triplicate. Survival analyses were performed and involved the following experimental conditions:

Nitroreductase

Tg(pkd2l1:GAL4, UAS:epNTR-tagRFPT-UTR.zb3) zebrafish embryos[51] and control sibling embryos were treated with 10 mM metronidazole (Sigma-Aldrich, M3761) in 0.1% DMSO (Sigma-Aldrich, D8418) for at least 16 hours to induce nitroreductase-mediated ablation of *pkd2l1*+ cells after mechanical dechorionation. At 2 dpf the larvae were washed 3 times with egg water and subsequently infected.

Botulinum toxin B Light Chain

Tg(pkd2l1:GAL4, UAS:BoTxBLC-GFP) zebrafish embryos[5,52,97] and control wild-type embryos were infected at 2 dpf.

Survival experiments in mutant larvae

Adult heterozygous zebrafish mutants (*pkd2l1*^{icm02}, *sgc2a*^{icm42}, *esm1*^{icm34}, *nppc*^{icm36}) were incrossed in order to compare survival between homozygous mutants and control siblings within the same clutches. Injection of *S. pneumoniae* targeted the hindbrain ventricle of 2 dpf zebrafish mutants and their control siblings (Figure S7) at different doses (1000 CFU or 2000 CFU per larva). We typically injected ~25 larvae for each CFU for each group in each experiment. The survival rate was evaluated every 12h until 72 hours post-infection (hpi) prior to genotyping after euthanasia of all larvae.

Analysis of calcium transients *in vivo*

To determine the overall activity of a given cell of interest defined within a region of interest (ROI), the ΔF/F integrated over time was calculated as it more reliable and less sensitive to fluctuations in the level of expression of the fluorescent calcium sensor; comparisons across conditions were made using multifactorial ANOVAs with Scheffé post-hoc tests. To compare isolated large-amplitude calcium transients (as in Figures 2E–2G and 2N), a MATLAB script was written to identify features of the Ca^{2+} trace where a sustained high-amplitude calcium transient (i.e. > 100% ΔF/F) was associated with a sharp onset (i.e. differential of ΔF/F trace > 30). Statistical testing was performed on these isolated events using the Wilcoxon rank sum test with Bonferroni correction for multiple comparisons.

Analysis of calcium transients *in vitro*

Slow translational drifts of the image due to cell movements were corrected using image registration by taking as a reference image a frame of the original position of the CSF-cN. We identified CSF-cN calcium transients in response to 1-second stimulus by using a 100 ms-long flash of green light performed 12.74s before the stimulus. Frames corresponding to flashes stimuli were removed from the representative traces (see Figures 3B and 3C). To determine the response of a given cell (ROI) to a 1-second stimulus (as in Figures 3D and 3E), the ΔF/F amplitude of each peak calcium response after stimulus was calculated using a home-made MATLAB script available on the Wyart lab github: the ΔF/F average of over six time points around the maximum ΔF/F of the peak was calculated, and was subtracted to this the ΔF/F average of six points before the stimulus. A cell was considered as a responding cell when we observed a response for at least one of the 3 1-second stimuli. Latency was calculated as time between the 1s-stimulus and the beginning of the peak response. Time-to-peak was calculated as the time between the beginning of the peak response and the maximum of the peak. Time decay was calculated by applying an exponential fit of model 'a*exp(-b*x)+c' and extracting the time decay as follow: decay = 1/b. As control for no-stimulus (see Figure 3G, black circles), we measured the time decay of transients corresponding to spontaneous activity with no stimulus (see Figures 3B and 3C, left). Comparisons across conditions (as in

Figures 3D and 3E) were made using 2-factor ANOVAs with Turkey HSD post-hoc tests on R. Comparisons for latency, time-to-peak and time decay were made using two-sample Kolmogorov-Smirnov non-parametric test on MATLAB.

Production of virus-containing supernatant

Sindbis virus (SINV)[76] was used to infect BHK cells. BHK-21 cells (ATCC #CCL-10) were cultured at 37°C and 5% CO2 in DMEM/F-12 containing phenol red (Gibco) supplemented with 5% heat-inactivated fetal bovine serum (Gibco) and penicillin-streptomycin (Life Technologies). To produce the supernatant, DMEM without phenol red was used instead. A near-confluent layer of cells in a 75cm^2 flask in 20 ml of culture medium was seeded with ~10^3 PFU of SINV-mCherry/2A virus, isogenic with the SINV-eGFP/2A virus whose construction is described in Boucontet et al.[98] and generated in the same way but replacing eGFP with mCherry. A control flask of BHK cells without virus was cultured in parallel. Two days later, supernatants were harvested and cell debris removed by centrifugation (5000 rpm, 10 min, 4°C). These supernatants were UV-inactivated by delivering 30mJ/cm^2 of 254 nm UV light using a CL-508 crosslinker (Uvitek). Titration on BHK cells ascertained that infective SINV particles fell from ~10^7 PFU/ml to zero after UV inactivation. Supernatants were frozen until use.

Analysis of neutrophil infiltration to the central canal after infection

Tg(mpo:GFP) transgenic larvae[83] expressing green fluorescent neutrophils were anesthetized and infected with 2000 CFU mCherry+ *S. pneumoniae* as described above or injected with 1 nl Alexa 647 Dextran (Thermo Scientific, D22914) in the hindbrain ventricle. After embedding the larvae in low-melting point agarose, time-lapse imaging was performed at 28°C on a Nikon AIR confocal microscope system equipped with a temperature-controlled chamber. Images were obtained at 20 min. intervals for 12-24 hours.

Behavioral analysis

Zebrafish larvae were either infected with 6000 CFU *S. pneumoniae* or injected with PBS at 5 dpf as above. Larvae were rested until 9, 24, or 32 hours post injection and plated individually in a 32 well (80 mm x 140 mm) made from 3 mm acrylic sheets (plexiglass) plate (BFP CINDAR, Champigny-sur-Marne, France) cut by a laser cutter into 1.5 cm diameter wells holding a volume of 500 μL. Larvae were then recorded freely for 5 minutes at 160 fps after 10 min of acclimation. Behavioral parameters were extracted using ZebraZoom.[99]

QUANTIFICATION AND STATISTICAL ANALYSIS

Behavioral analysis

Behavioral parameters were extracted from tracking videos as previously described.[99] These were tested across time points and conditions using a 2-factor ANOVA followed by Scheffé post-hoc testing.

Quantification and analysis of axial curvature and fluorescence

Following injection and imaging, the spinal cord was manually delineated using MATLAB (*curvature.m*, *linecurvature2D.m*).[8] This produced an imaging area from which curvature was calculated from a smoothing spline curve fit to the x-axis boundaries and total 568 nm fluorescence was integrated across the x-axis. We therefore obtained both a total fluorescence and local curvature for each spinal cord; curvature was compared via a Student's t-test (Figure 1R) while curvature and fluorescence were correlated by simple linear regression (Figure 1S).

In vivo calcium imaging

Large ΔF/F events were detected using a MATLAB algorithm. These large events were effectively filtered for those where—

- Amplitude > 100% ΔF/F
- Initial first differential of ΔF/F > 30%/frame

These criteria were effectively used to threshold a series of time points where ΔF/F rose very rapidly to high levels; *strel()* and *imclose()* functions were then used to smooth those thresholded points into continuous intervals (for further details, see *super.m* in the referenced GitHub repository).

After filtering, these events were tabulated by time point and condition and evaluated for each experiment by 2-factor ANOVA followed by Scheffé post-hoc testing to find time-point-specific differences. The exception to this was in Figures 2I and 2J, where large events for most conditions were so infrequent as to not be statistically comparable; we therefore used chi-square analysis here to show that large events were more common in the live *S. pn*. condition than other conditions.

RNAseq

For the initial transcriptome (Figure 4) RNAseq reads were mapped to the zebrafish GRCz10 genome draft and evaluated for enrichment by evaluating false discovery rate of log fold change for fragments per kilobase of transcript per million fragments mapped (FPKM).

In vitro calcium imaging

Image registration was carried out using as image of reference a frame of the original position of the CSF-cN; this was used to correct small cell movements occurring during calcium imaging *in vitro*. To synchronize the 1-second stimulus on the cell with the calcium imaging movie recording, we used a 100 ms-long flash of green light (detectable on the calcium imaging movie) performed exactly 12.74 seconds before the stimulus. We removed frames corresponding to flash stimuli from the representative traces.

Quantification of the amplitude of CSF-cN calcium responses to 1-second stimuli was performed by calculating the ΔF/F amplitude of each peak calcium response after each stimulus using a home-made MATLAB script (see *Analyse_amplitudesV5.m* available on the Wyart lab GitHub repository). This script calculated the ΔF/F average of over six time points around the maximum ΔF/F of the peak, and subtracted to this the ΔF/F average of six points before the stimulus. We considered a cell responding to at least one of the three 1-second stimuli as a responding cell.

Quantification of latency was performed by calculating the time between the 1-second stimulus and the beginning of a peak response.

Quantification of time-to-peak was performed by calculating the time between the beginning of the peak response and the maximum of the peak.

Quantification of time decay was performed using a home-made MATLAB script (see *Analyse_kinematicsV3.m* available on the Wyart lab GitHub repository) applying an exponential fit of model 'a*exp(-b*x)+c' and extracting the time decay as follow: decay = 1/b. No-stimulus control (see Figure 3G, black circles) time decay was measured using the time decay of transients corresponding to spontaneous activity with no stimulus (see Figures 3B and 3C, left).

Statistics of comparisons across conditions (as in Figures 3D and 3E) were performed using 2-factor ANOVAs with Turkey HSD post-hoc tests on R, with the exception of *S. pneumoniae* supernatant experiment *in vitro* (Figures 7A and 7B) which was analyzed using paired t-test. Statistics of comparisons for latency, time-to-peak and time decay were made using two-sample Kolmogorov-Smirnov non-parametric test in MATLAB (see GitHub repository).

Survival analysis

All survival data were analyzed by log-rank test (Mantel-Cox). All data were analyzed by Student's t-test for comparison of two groups or two-way ANOVA followed by Sidak's or Tukey's post hoc test. Bacterial load and competitive index data were analyzed by unpaired t-test or one sample t-test respectively. The number of subjects and biological replicates is indicated in the figure legends. All data including error bars are presented as mean ± SD or mean ± SEM. *P value*s <0.05 were considered statistically significant, unless stated otherwise. All statistical analyses were performed using MATLAB or GraphPad Prism 7.0.